The Electronic Structure of the Tyr-Cys· Free Radical in Galactose Oxidase Determined by EPR Spectroscopy

Yuk Ki Lee

B.S. Biochemistry. University of Oregon (2005)

A thesis presented to the faculty of the

OGI School of Science & Engineering

at Oregon Health and Science University

in partial fulfillment of the

requirements for the degree

Master of Science

in

Environmental and Biomolecular Systems

September 2007

The thesis "The Electronic Structure of the Tyr-Cys· Free Radical in Galactose Oxidase Determined by EPR Spectroscopy" by Yuk Ki Lee has been examined and approved by the following Examination Committee:

Dr. James W. Whittaker
Associate Professor
Thesis Advisor

Dr. Bradley M. Tebo
Professor

Dr. Pierre Moënne-Loccoz
Associate Professor

ACKNOWLEDGEMENTS

I would like to thank my advisor, Dr. James Whittaker for his support and encouragement throughout my research project. His helpful advices help me to complete my thesis in a much easier way. I also want to thank him for giving me a chance to work in his lab and learn from him.

I would also like to thank Mei Whittaker for preparing the protein samples for my experiments and giving advices on my thesis.

I thank all of my committee members, Dr. James Whittaker, Dr. Bradley Tebo, and Dr. Pierre Moënne Loccoz for reviewing my thesis and providing their recommendations.

I am so thankful that my parents and my sister are always so encouraging and supportive in the last two years. I would like to thank them for always being there for me every time I face a challenge.

CONTENTS

LIST OF FIGURES

LIST OF TABLES

ABSTRACT

The Electronic Structure of the Tyr-Cys· Free Radical in Galactose Oxidase Determined by EPR Spectroscopy

Yuk Ki Lee, B.S.

M.S., OGI School of Science & Engineering
at Oregon Health & Science University

September 2007
Thesis Advisor: Dr. James W. Whittaker

The EPR spectrum of the Tyr-Cys· free radical in oxidized apoGAOX has been investigated, using a combination of approaches. Power saturation analysis has been used to resolve two unique spectra through Evolving Factor Analysis (EFA) global fitting, indicating the presence of two distinct free radical species in the sample. The component that dominates at low microwave power arises from the Tyr-Cys· side chain, while the high power component has not yet been assigned. The experimental results show that the EPR spectrum collected at low power includes approximately 7% of the high power component. EPR spectra have been collected for ten different isotope derivatives of GAOX, including ^{2}H-labeled, ^{13}C-labeled, ^{17}O-labeled, and ^{33}S-labeled forms. XSophe simulation of the EPR spectra has been performed for the isotopically labeled samples in order to determine the spectroscopic parameters – g-values, hyperfine coupling constants, and linewidths. The g-values and the methylene proton hyperfine coupling constants obtained for the isotopically labeled samples are consistent with the literature values. The magnitude of the hyperfine coupling constants associated with each of the nuclei confirms that significant electron spin density is found on the methylene protons, the alternating carbon atoms within the aromatic π system and the $2p_z$ orbital of both sulfur and oxygen. Moreover, the rotation angle of the methylene protons to the phenoxyl ring around the C1-C7 bond has been evaluated based on the experimentally defined hyperfine coupling constants of the two methylene protons.

CHAPTER 1
INTRODUCTION

1.1 The Biological Importance of Free Radicals

Free radicals are chemical species containing one or more unpaired electrons in their valence shell. These unpaired electrons make them highly reactive, and they are generally assumed to be harmful to living cells. This view is certainly justified. However, even though reactive free radicals can damage nucleic acids, breaking the strands and modifying the bases, resulting in mutation and even cancer, they are also involved in essential biological processes. Some radical species, such as ·NO, act as intracellular messengers for signal transduction (1). Other radical species perform catalytic roles in the active site of free radical enzymes (1). Biological free radicals that are involved in enzymatic catalysis are often associated with specialized redox sites in enzymes. For example, radicals are stabilized on a Tyr residue (Y122) of type I ribonucleotide reductase, a Tyr residue (Y_Z) of photosystem II (2), a Trp residue (W191) of cytochrome *c* peroxidase (3), and a Tyr residue (Y272) of galactose oxidase (GAOX) (4). Free radicals localized on tyrosine side chain are related to phenoxyl free radicals (Figure 1.1) where the unpaired electron is delocalized over the aromatic ring and oxygen of the amino acid side chain. Electron paramagnetic resonance (EPR) spectroscopy (described in more detail below) is a powerful tool for studying the electronic structure of these free radicals. The present work describes a detailed EPR analysis of the free radical site in GAOX.

1.2 Galactose Oxidase

1.2.1 Biological Background

GAOX is a 68 kDa monomeric copper metalloenzyme, secreted by a filamentous fungus (*Dactylium dendroides*) into the extracellular space. The biological function of GAOX has not been clearly established, but it is able to catalyze the oxidation of a wide range of primary alcohols to aldehydes, coupling alcohol oxidation to reduction of dioxygen to hydrogen peroxide. Hydrogen peroxide may serve as fuel for extracellular peroxidases or as an agent for killing bacteria. The two catalytic half reactions are:

Oxidation: $RCH_2OH \rightarrow RCHO + 2e^- + 2H^+$ (1)

Reduction: $O_2 + 2e^- + 2H^+ \rightarrow H_2O_2$ (2)

Alcohol oxidation is regioselective, and no secondary alcohols are oxidized. However, GAOX can oxidize a wide range of primary alcohols, including simple sugars, aliphatic and aromatic alcohols, and even protein glycoconjugates (5). This primary alcohol specificity is due to the bulky side chains that coordinate with the metal center in the active site (described in more detail below). Therefore, the larger secondary alcohols cannot enter the active site and undergo oxidation.

1.2.2 Protein Structure

GAOX is expressed as a 680 residue precursor polypeptide containing an N-terminal prepro signal sequence that directs secretion of GAOX into the extracellular space. The precursor protein is processed by proteolytic cleavage to yield the 639 residue mature GAOX (9). The structure of the mature protein has been solved by X-ray crystallography (8). The mature protein is composed of three structural domains consisting almost entirely of β strands and short turns (Figure 1.2a). The N-terminal domain (Residues 1-154) consists of 8 strands of antiparallel β sheet folded into a sandwich structure. It contains a metal binding site formed by Asp32, Asn34, Thr37, and Glu142 predicted to be a Ca^{2+} binding site (5) as well as a noncatalytic carbohydrate

binding site that may target the enzyme to the extracellular carbohydrates (7). The active site of GAOX is located in the catalytic domain (Residues 155-552), which folds into a 7-fold β propeller structure that binds the catalytic copper ion (Figure 1.2b). This domain belongs to the *kelch* superfamily of protein fold (7) and the propeller domain contains 6 four-stranded antiparallel β sheet subdomains followed by a seventh domain containing only three-stranded antiparallel β sheet. The latter is completed by a short β strand that precedes the first *kelch* module, linking the ends. The C-terminal domain (Residues 553-639) caps the propeller and contributes one of the metal ligands (His581) to the copper binding site, which lies on the axis of the β propeller.

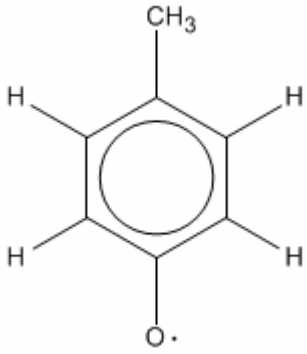

Figure 1.1 Structure of a simple phenoxyl free radical.

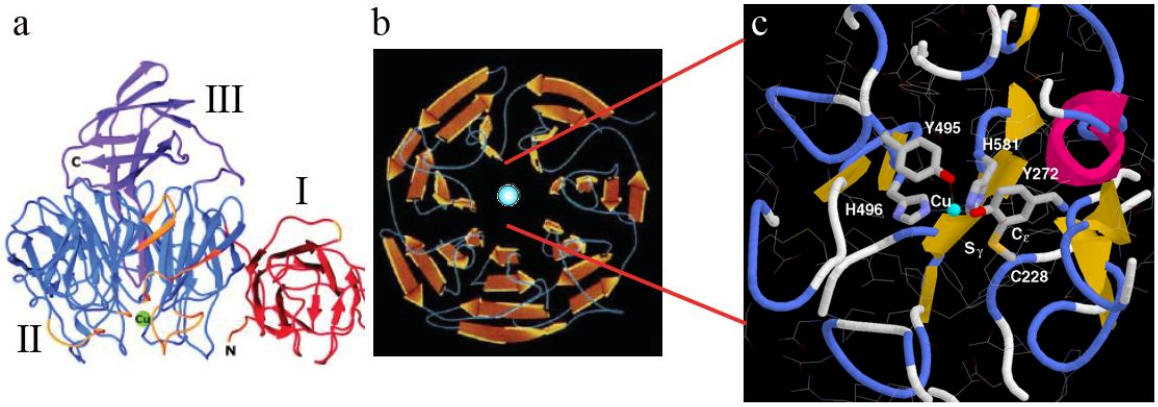

Figure 1.2 a) The structure of GAOX. Three domains of GAOX are shown in different colors with a green sphere at the catalytic domain represents the copper ion Domain I is the N-terminal domain, Domain II is the catalytic domain, and Domain III is the C-terminal Domain(6). **b)** The catalytic domain of GAOX folds into a 7-fold β propeller structure that contains the catalytic copper binding site. The sphere is the center represents the copper ion (8). **c)** The zoom-in structure of the copper binding site (9).

1.2.3 Active Site

In the active site of GAOX (Figure 1.2c), Cu(II) ion coordinates to five ligand residues - Tyr495, Tyr272, His496, His581 and a solvent molecule, forming a distorted square-pyramidal complex (Figure 1.3). However, reduction of Cu(II) gives rise to Cu(I)-containing GAOX, which coordinated to Tyr272, His496 and His581 to form a trigonal planar complex. The interconversion between Cu(I) and Cu(II) oxidation states contributes one electron to the enzymatic catalysis by GAOX. The second electron required for the catalysis comes from one of the ligand residues – Tyr272. A unique post-translational modification occurs spontaneously to Tyr272 in the active site during protein biosynthesis in the presence of copper and dioxygen, but in the absence of any other protein (9), resulting in the formation of an unusual covalent linkage between the ring carbon of Tyr272 ortho to the phenol oxygen and the sulfur atom of the Cys228 side chain, forming a tyrosyl-cysteine cross-link (Figure 1.4). The formation of this Tyr-Cys cross-link is directed by the active site and is required for the enzymatic activity of GAOX because the thioether bond gives Tyr272 its distinctive redox reactivity. The Tyr-Cys side chain can form a protein free radical by mild oxidation. This observation, as well as extensive spectroscopic characterization identifies it as the protein free radical site in GAOX. By analogy to well characterized phenoxyl free radicals, the unpaired electron in the Tyr-Cys· free radical is expected to be delocalized over the aromatic ring of Tyr272, mainly on the alternating atoms within the aromatic π system, with a significant unpaired electron density on Tyr phenoxyl oxygen (7) (Figure 1.5). Computational studies have also predicted a significant (10-25%) localization of unpaired electron density on the thioether sulfur. The free radical Tyr-Cys ligand, which functions as a redox cofactor, strongly interacts with the redox active copper metal center in the active site, forming a two-electron redox unit. This unique catalytic active site combines the reactivity of a free radical with the redox chemistry of a copper ion, a catalytic motif that is the basis for a family of enzymes called radical copper oxidase. GAOX is the best characterized of these radical copper oxidases.

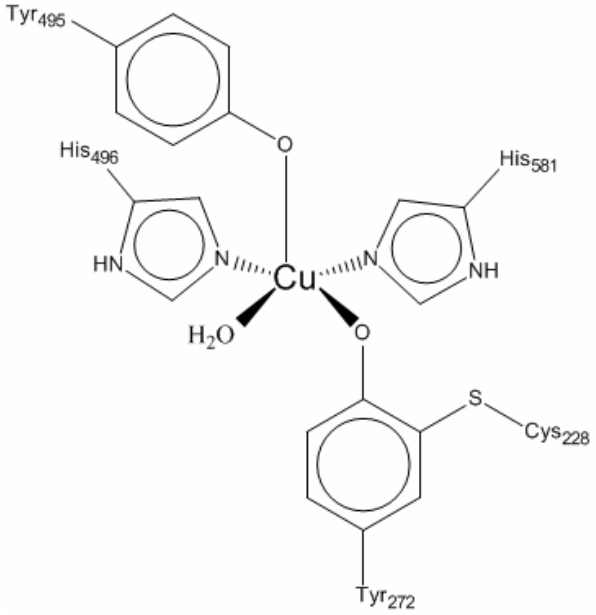

Figure 1.3 Active site of GAOX with Cu(II) (10).

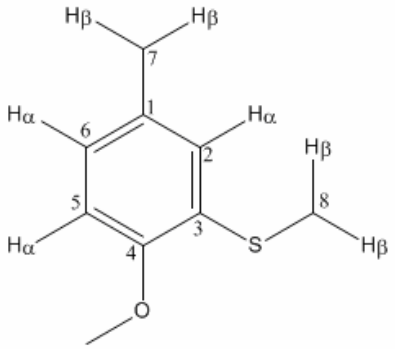

Figure 1.4 Structure of Tyr-Cys Cross-link.

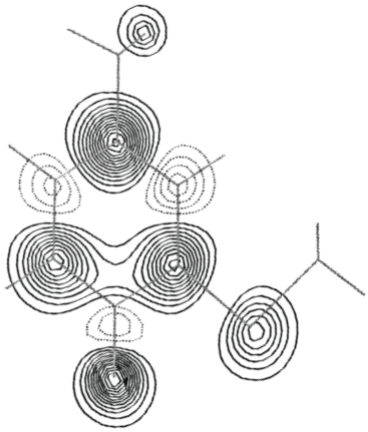

Figure 1.5 Electronic structure of Tyr-Cys side chain in GAOX. Unpaired electron delocalizes over the aromatic ring of Tyr, mainly on the alternating atoms within the aromatic π system, with a significant unpaired electron density on Tyr phenoxyl oxygen and Cys sulfur. It is based on a figure by Whittaker, 2002 (7).

1.2.4 Redox Forms of GAOX and ApoGAOX

GAOX can be prepared in three distinct redox forms. The fully oxidized (AGO) and the fully reduced (RGO) forms are catalytically active while the one-electron reduced (IAGO) form is catalytically inactive (Figure 1.6a) (7). The green, fully oxidized form contains a Cu(II) center coupled to a Tyr-Cys· free radical. Addition of one electron to the free radical site of AGO results in the conversion to the inactive, blue IAGO form, which contains Cu(II) but no radical. Further reduction gives rise to the colorless RGO form, which contains Cu(I) center. The AGO form reacts with primary alcohols and is converted to RGO by accepting two electrons from the substrate while RGO can react with dioxygen and convert itself back to AGO by donating its two electrons to O_2.

In the AGO complex, the Tyr-Cys· free radical (S = ½) is coupled to the $3d^9$ Cu(II) metal ion (S = ½). The antiferromagnetic coupling between Cu^{2+} and the free radical results in a total spin $S_T = 0$ (EPR silent). An excited triplet state (total spin $S_T = 1$) resulting from parallel alignment of the two spins occurs at higher energy (5). However, no EPR signal has been detected for the triplet state. Both the antiferromagnetic ground state and the excited triplet state give no observable EPR signal, so EPR signal from the free radical in GAOX can only be observed in metal-free apoenzyme.

Apoprotein is a protein without the prosthetic group. In our study, apoGAOX lacks the paramagnetic Cu metal ion, allowing us to detect an EPR signal arising from the Tyr-Cys· free radical in the enzyme. Because the redox active copper is missing, there are only two redox states assemble to apoGAOX (Figure 1.6b). Apo-ox is the oxidized form, having a Tyr-Cys· free radical. Addition of one electron will lead to the formation of one electron reduced apoGAOX (Apo-red) with no free radical.

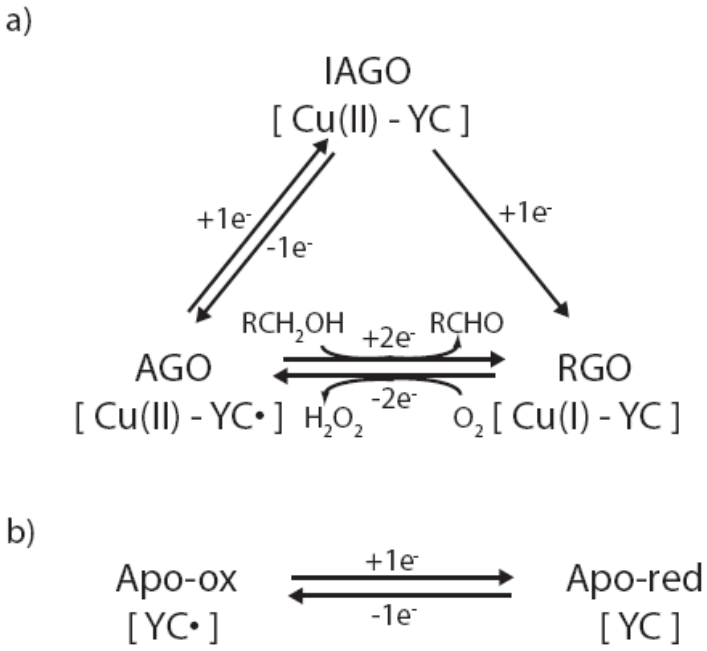

Figure 1.6 a) Three redox forms of GAOX and their interconversion. Only AGO (fully oxidized) and RGO (fully reduced) forms are catalytically active. **b)** Interconversion of the two redox forms of apoGAOX.

1.3 EPR Spectroscopy

1.3.1 Introduction

Electron paramagnetic resonance (EPR) spectroscopy, also known as electron spin resonance (ESR), is a physical technique for detecting the unpaired electrons in a sample. The information contained in EPR spectra can be used to determine the identity of these paramagnetic species and to investigate their molecular electronic structure. An electron has an intrinsic spin $S = ½$. In an electron pair as found in a filled molecular orbital, the spins of the paired electrons cancel ($S_T = 0$) and most organic molecules are diamagnetic. In contrast, the uncompensated spin of an unpaired electron in a free radical allows it to be sensitively detected by EPR spectroscopy.

1.3.2 Zeeman Effect

In an EPR experiment, magnetic field is applied to the radical species in the resonance cavity, causing Zeeman Effect, which is an interaction between the magnetic moment of a spin ($S = ½$) and the magnetic field, which gives rise to two electronic spin states ($M_s = +½, -½$) at different energies (Figure 1.7). When electromagnetic radiation of microwave frequency is applied to the sample, transitions between the excited state and the ground state are induced if the energy level separation between the two energy states matches with the energy of incident radiation. EPR spectroscopy is able to detect this resonant absorption of radiation, and produce an EPR spectrum. The resonance condition is given by:

$$\Delta E = h\nu = g\beta H_{res} \qquad (3)$$

where ΔE is the energy level separation, h is the Planck constant (6.626×10^{-34} J•s), ν is the frequency of the applied radiation, g is the electron g-factor (2.0023), β is the Bohr magneton (0.92×10^{-23} J•T) and H_{res} is the applied magnetic field at resonance.

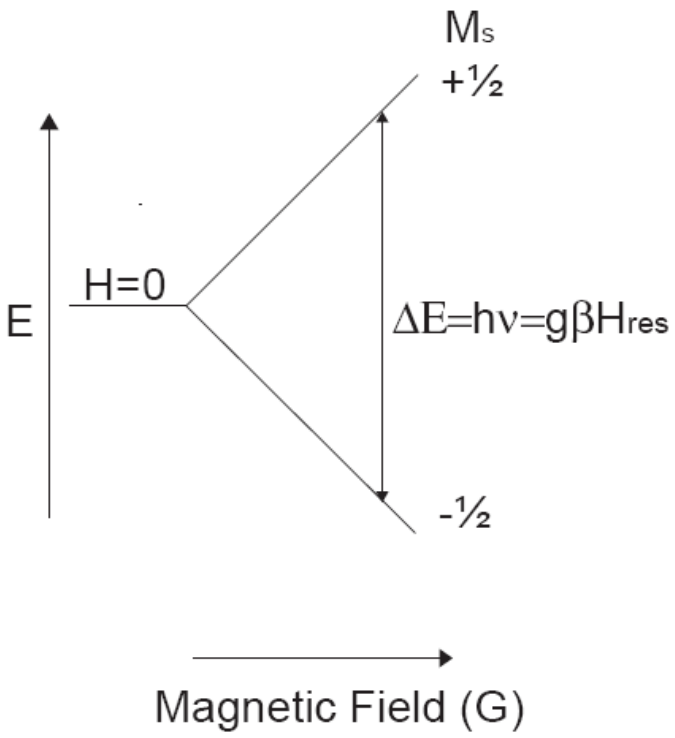

Figure 1.7 Zeeman effect illustration. Energy difference between two energy levels of an unpaired electron ($S = ½$) in an applied magnetic field due to Zeeman effect.

The major disadvantage of EPR spectroscopy is the contribution of noise to the output signal at low frequencies. However, the signal-to-noise ratio can be improved by small amplitude field modulation (11) (Figure 1.8). Two Helmholtz coils, which are driven by an oscillator, are placed on either side of the cavity, producing an AC signal at modulation frequency (100kHz) that can either subtract from (when the two signals are opposite in phase) or add to (when the two signals are in phase) the amplified detected signal. A phase-sensitive detector, also known as a lock-in-amplifier, can be used to filter out all signals other than that modulated at 100kHz (12). Modulation of the magnetic field generates a first derivative signal, which is proportional to the slope of the absorption curve (Figure 1.8). In order to prevent the distortion of the signal line shape, modulation amplitude is usually chosen to be smaller than the line width (see Spectral Parameters).

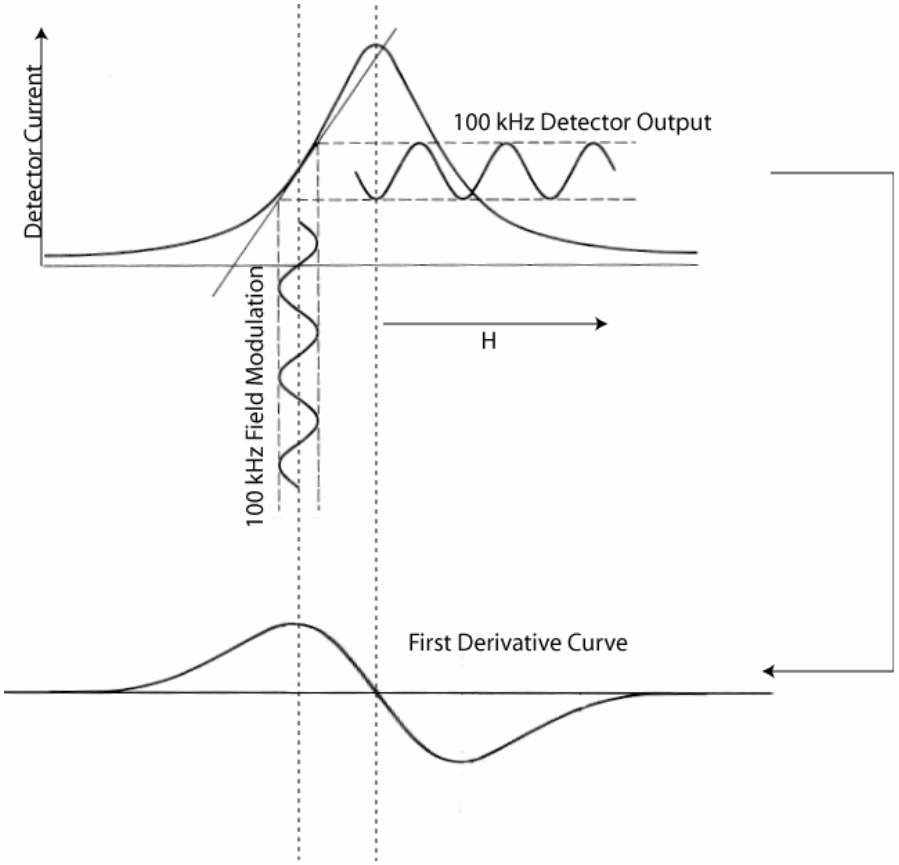

Figure 1.8 Field modulation illustration.100kHz field modulation generates a first derivative output signal detected by a phase-sensitive detector. It is based on figures by Wertz and Bolton, 1972 (11).

1.3.3 Spectral Parameters

There are four major parameters - intensity, g-value, hyperfine coupling constant and linewidth - that are used to describe an EPR spectrum. The integrated intensity gives the information about the concentration of radical species in the sample. The g-value contains information about the electronic structure of the species. From Equation (3), the g-value can be empirically defined as:

$$g = h\nu / \beta H_{res} \tag{4}$$

The measurement of the g-value can aid in the identification of an unknown species. The g-tensor is composed of three principal components: g_x, g_y and g_z. When the g-values, g_x, g_y and g_z, are isotropic ($g_x = g_y = g_z$), the spectrum is independent of the orientation of molecule in the magnetic field at resonance. In contrast, when the g-value is anisotropic, g_x, g_y and g_z are distinct and can have an axial symmetry with $g_x = g_y \neq g_z$ or rhombic symmetry with $g_x \neq g_y \neq g_z$.

Hyperfine coupling occurs when the magnetic moment of the unpaired electron spin interacts with that of a nuclear spin in a system containing nuclei with $I > 0$ (Table 1.1). There are two kinds of interaction between the electron and nuclear spins. The first interaction, which results from the unpaired spin density at the nucleus, gives rise to isotropic hyperfine coupling ($A_x = A_y = A_z$). The second interaction, which results from the dipolar interaction between electron and the nuclear magnetic moments, gives rise to anisotropic hyperfine coupling (axial: $A_x = A_y \neq Az$, or rhombic: $Ax \neq A_y \neq A_z$). When the nuclear magnetic moment interacts with the electron magnetic moment, nuclear spin is actually producing a local field at the electron, which gives rise to $(2I + 1)$ energy levels and EPR spectrum is split into $(2I + 1)$ lines. More generally, for n equivalent nuclei, $(2nI + 1)$ lines will be observed. If the unpaired electron interacts with several non-equivalent nuclei, the number of peaks expected is obtained by taking the products of $(2nI + 1)$ for each nucleus. Selection rules $\Delta M_s = \pm 1$ and $\Delta M_I = 0$ are used to determine which transitions will be detected by EPR spectroscopy. From Figure 1.7, the Zeeman Effect of an unpaired electron in the magnetic field will only produce two energy levels between which one transition will occur. In contrast, hyperfine coupling between a

nucleus with $I = ½$ and an electron with $S = ½$ will give rise to four energy levels and two transitions will be detected by EPR spectroscopy (Figure 1.9). Moreover, due to the presence of the hyperfine interaction, the resonance condition (13) is described by Equation (3) with an extra term:

$$\Delta E = h\nu = g\beta H_{res} + AM_I \quad (5)$$

where A is the hyperfine coupling constant and M_I is the nuclear magnetic quantum number.

Table 1.1 Isotopes with their spins and magnetogyric ratios.

Isotopes	Spin (I)	Magnetogyric Ratio (γ) [10^7 rad s^{-1} T^{-1}]
^{1}H	½	26.75
^{2}H	1	4.11
^{12}C	0	-
^{13}C	½	6.73
^{32}S	0	-
^{33}S	3/2	2.06
^{16}O	0	-
^{17}O	5/2	-3.62

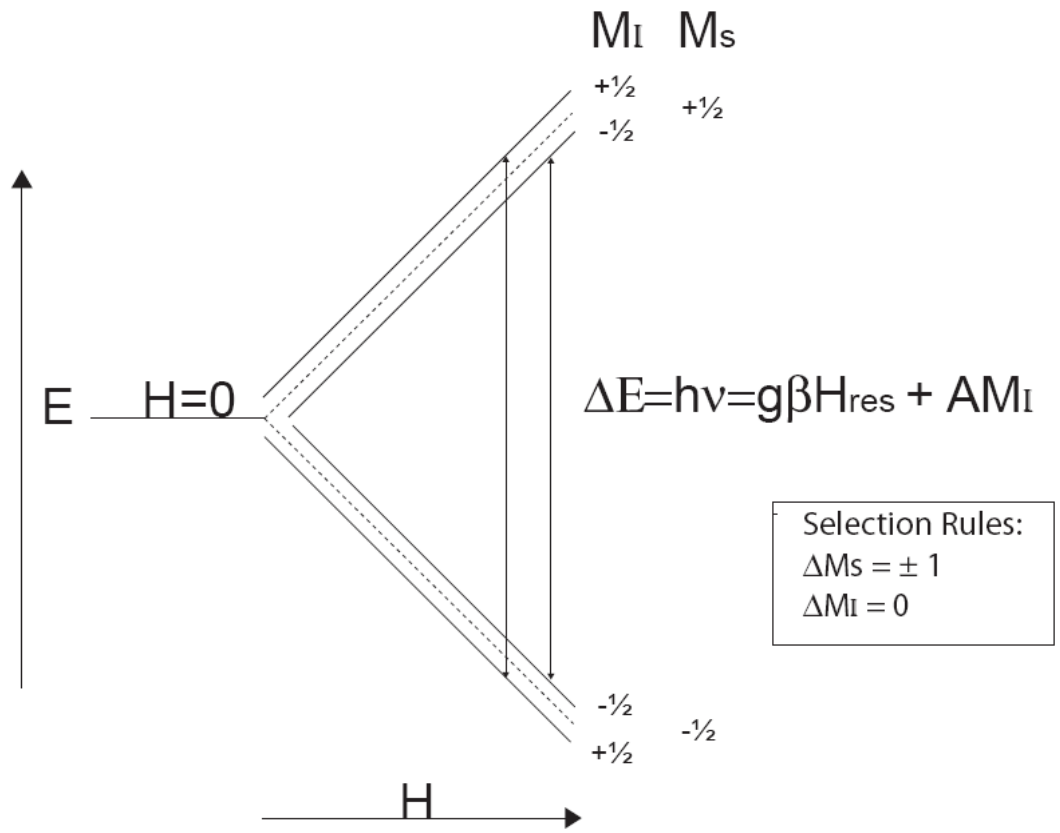

Figure 1.9 Hyperfine coupling illustration. Energy-level splitting due to the hyperfine coupling between a nucleus ($I = ½$) and an unpaired electron.

The linewidth of an EPR spectrum is related to the relaxation times. The first contribution to the linewidth is the spin-lattice relaxation time (T_1) – the lifetime of the spin states. Shorter T_1 give broader linewidth as a result of lifetime broadening. The second contribution to the linewidth is the inhomogeneous broadening, arising from the different magnetic fields experienced by each paramagnetic center in the randomly oriented frozen solution. However, if all the paramagnetic centers are identical and they resonate at the same magnetic field, homogeneously broadening will occur. Usually inhomogeneously broadened lines give Gaussian lineshape while homogeneously broadened lines give Lorentzian lineshape (14). The linewidth of a spectrum is also related to power saturation through the spin-lattice relaxation time. EPR signal amplitude is proportional to the square root of incident microwave power below saturation. However, the signal amplitude will decrease with increasing power when saturation occurs, because the increased microwave power will increase the rate of transition between the two energy levels, causing the spin lifetime to reduce, leading to line broadening. In a power saturation experiment, a series of spectra are collected with increasing microwave power and the signal intensity for each spectrum is recorded. A plot of *log* (*Signal Intensity* / √*Microwave Power*) vs. microwave power will have two regions, saturating and nonsaturating. In the nonsaturating region, the plot is a horizontal straight line. When the signal starts to saturate, the plot curves down. The intersection of these two regions can be used to determine $P_{½}$, the microwave power required for half saturation.

Since different samples saturate at different microwave powers, each sample should be studied at different power level in order to determine its power saturation properties and select the best operational power for that sample.

1.3.4 EPR Properties of Tyrosyl Free Radicals

The aromatic ring of a Tyr free radical contains a methylene group at the C1 position and an oxygen at the C4 position with its unpaired electron is delocalized over the aromatic ring (Figure 1.10a). The hyperfine splitting is mainly due to interaction of

the unpaired electron spin with the nuclear spin of two methylene protons (H_β). Since the 2p orbital of the aromatic ring carbon (C1) overlaps with the 2p orbital of C7 and the latter orbital overlaps with the 1s orbital of the methylene proton, allowing the unpaired electron spin to interact, resulting in hyperfine coupling. The magnitude of the hyperfine interaction depends on the rotation angle between the 2p orbital of C1 and the methylene protons on C7 (Figure 1.10b). The hyperfine coupling will be maximum if the rotation angle (θ) is 0 or $n\pi$ while it will be minimum if the rotation angle is $(n/2)\pi$ (n is an integer).

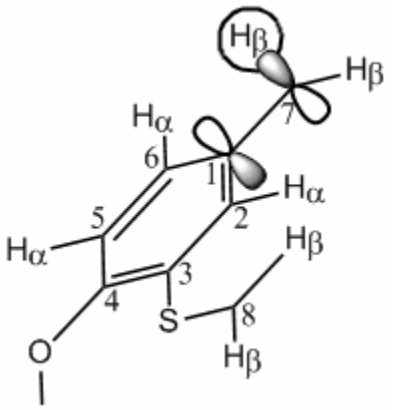

Figure 1.10a Overlapping orbitals of C1, C7, and methylene protons.

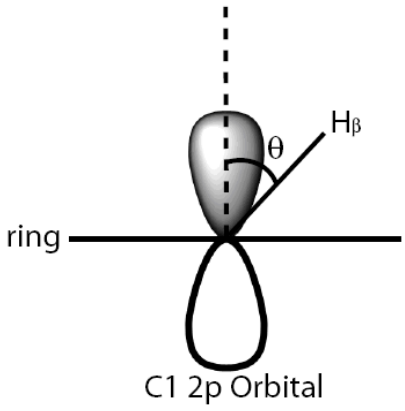

Figure 1.10b Rotation angle (θ) between 2p orbital of C1 and 1s orbital of methylene proton on C7.

1.4 *Isotopic Labeling*

Isotopic labeling is useful for analyzing complex EPR spectra, to determine accurate g-values and the spin density distribution in molecules without changing the electronic structure or the chemistry of the site. For example, when a proton (^{1}H) is replaced by deuterium (^{2}H) in a molecule, the smaller magnetic moment associated with ^{2}H results in a smaller hyperfine splitting, essentially decreasing the contribution of that nucleus to the EPR spectrum. On the other hand, when ^{12}C ($I = 0$) is replaced by ^{13}C ($I =$ ½), or ^{32}S ($I = 0$) is replaced by ^{33}S ($I = 3/2$), or ^{16}O ($I = 0$) is replaced by ^{17}O ($I = 5/2$), it can give rise to new hyperfine coupling effects that aid in localizing the distribution of the unpaired electron. Therefore, in addition to unlabeled Tyr-Cys· oxidized apoGAOX, ^{2}H-labeled, ^{13}C-labeled, ^{17}O-labeled Tyr and ^{33}S labeled Cys oxidized apoGAOX were also prepared. In order to prepare these isotopically labeled enzymes, a high-level expression host – *Pichia pastoris* (methylotropic yeast) is used (15). An auxotrophic expression strain of *P. pastoris* containing an engineered defect in *TYR1* gene, was generated by the *ura3* deletion cassette method using standard recombination techniques (Figure 1.11a). This Tyr auxotroph strains was made electrocompetent and transformed with an expression cassette (pPICZαGAOX), containing pPICZα expression vector, *Saccharomyces cerevisiae* α-mating factor leader peptide (α-MF) ligated to mature protein sequence of *D. dendroides* GAOX. The expression of recombinant GAOX can be induced by high-density fermentation with methanol and different labeled Tyr (15). Since this auxotrophic stain absolutely requires tyrosines for growth, so the protein will incorporate the exogenously added labeled Tyr, allowing isolation of isotopic variants of GAOX. The effect of isotope substitution can be determined by quantitative EPR spectroscopy.

The aim of our work is to experimentally determine the unpaired electron distribution in the delocalized Tyr-Cys· Free radical over all of the atoms in the Tyr-Cys side chain.

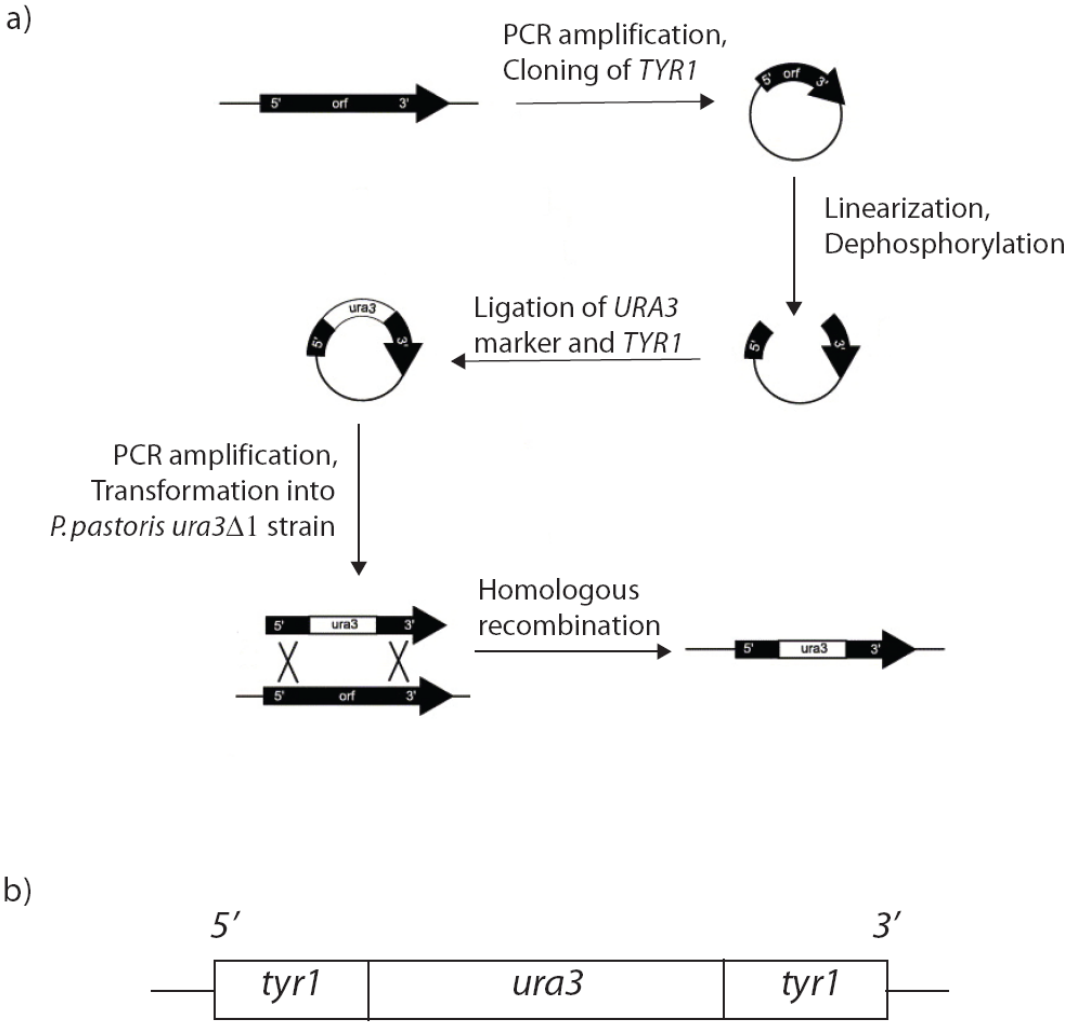

Figure 1.11 a) Procedure for the production of *TYR1* disruption cassette (9). **b)** *TYR1* disruption cassette with *URA3* selection marker in the middle (9).

CHAPTER 2
MATERIALS AND METHODS

2.1 Reagents

L-Tyrosine was purchased from sigma (St. Louis, MO). L-Tyrosine-3,3-d_2 (99.84 atom % D) was obtained from Sigma-Aldrich Milwaukee, WI). L-Tyrosine ring-3,5-d_2 (≥98 atom % D) was purchased from Cambridge Isotope Laboratories (Andover, MA). Fully deuterated Tyrosine (DL-4-hydroxyphenyl-d_4-alanine-2,3,3-d_3, 99.2 atom % D) and DL-Tyrosine ring-2,6-d_2 (DL-4-hydroxyphenyl-2,6-d_2-alanine-2-d_1, 98.1 atom % D) were obtained from CDN Isotopes (Pointe-Claire, Quebec). DL-Tyrosine ring deuterated (DL-2,2,3,5,6-d_5 Tyrosine, 97 atom % D) was synthesized as described by published procedures (16), except the reaction was done under argon at 145-150^{o}C for two days and at the end of the reaction, the reaction mixture was adjusted to pH 4.5 with concentrated NH_4OH in an ice bath. The exchange reaction was repeated with the product from the first reaction. ^{13}C-labeled L-Tyrosines were purchased from Cambridge Isotope Laboratories: phenol-4-^{13}C, phenol-3, 5-$^{13}C_2$, and ring-$^{13}C_6$ (≥98 atom %^{13}C). ^{17}O-labeled L-Tyrosine (L-4-hydroxy-^{17}O-phenyl alanine, 50 atom % ^{17}O) was obtained from Isotec (Miamisburg, OH). ^{33}S metal (≥98 atom % ^{33}S) was obtained from Cambridge Isotope Laboratories. ^{33}S was oxidized to sulfate, and added to the growth media for expression of ^{33}S-labeled galactose oxidase.

2.2 Media and Growth Conditions

Standard defined (SD) medium is the minimal medium, containing only Yeast Nitrogen Base (YNB), ammonium sulfate and some PTM4 trace metals (17). Maintenance of *P. pastoris* Tyr^- stains and production of recombinant GAOX were performed in SD medium, supplemented with tyrosine (150mg/L).

2.3 Protein Expression

Electrocompetent cells were prepared for a tyrosine auxotroph strain (*TYR1* is the tyrosine biosynthetic gene coding for prephenate dehydrogenase) of *P. pastoris* from 500mL of culture in phosphate-buffered SD medium, 2% glucose and supplemented with tyrosine (15). The cells were transformed with 4μg of *Pme* I-linearized pPICZαGAOX expression vector by electroporation. 1mL cold 1M sorbitol was added immediately to the mixture and the solution was transferred to 14mL Falcon tubes for incubation at 30°C with shaking for 1 hour. 1mL SD medium containing 1M sorbitol was added and shaking continued for another hour. Selection was performed on agar plate with SD medium, glucose, supplemented with tyrosine and antibiotic Zeocin for killing off all the cells that lack the αGAOX expression cassette. The largest colonies grown on the agar plate were plated onto expression medium with unlabeled tyrosine to confirm the expression of recombinant GAOX. Labeled GAOX was synthesized with the labeled tyrosines. 20mL of phosphate-buffered SD with 2% glucose supplemented with 150mg/L unlabeled tyrosines were inoculated in a 125mL baffled flask using freshly grown expression strain culture and grown at 30°C with shaking. The culture was centrifuged in sterile Oak Ridge tubes and the cells were resuspended in 1L 2× phosphate-buffered SD with 2% glucose and labeled amino acid plus 1mL PTM4 and 2mL 0.02% biotin in a 2L baffled flask. Culture was allowed to grow at 30°C with shaking until it reached stationary phase. Cells were centrifuged and resuspended in 200mL 2× phosphate buffered SD with PTM4 trace metals solution, 2mL 0.02% biotin, 20μM $CuSO_4$ and labeled amino acid in a 2L baffled flask. Galactose oxidase expression was induced with 0.05% methanol added daily for 4

days at 30°C with shaking (15). The expression constructs for the wild type strain was prepared using the standard method (18) by transforming the electrocompetent cells in wild type strain of *P. pastoris* with pPICZαGAOX expression vector.

2.4 *Oxidized ApoGAOX Preparations*

Pichia cell biomass was removed from the fermentation culture and GAOX was purified according to the published procedures (18). The metal-free apoGAOX was prepared by a modified chelation procedure (19, 20). A concentrated diethyldithiocarbamate solution was added to 0.5mM GAOX solution with an 8-fold excess. The yellow mixture was centrifuged at high speed, leaving a colorless supernatant and unreacted reagent was removed by gel filtration. Oxidized apoGAOX was prepared by adding 50mM $K_3Fe(CN)_6$ to the metal-free enzyme and the oxidant was removed by desalting.

2.5 *Spin Quantitation*

The concentration of the free radical in a protein sample can be calculated through comparison with the 1mM Spin standard – $Cu(ClO_4)_2$ based on this equation:

$$C_{spin} = \frac{\iint I_{spin}}{\iint I_{s\tan dard}} \times \frac{H_{\mathrm{mod},s\tan dard}}{H_{\mathrm{mod},spin}} \times \frac{T_{spin}}{T_{s\tan dard}} \times \sqrt{\frac{P_{s\tan dard}}{P_{spin}}} \times C_{s\tan dard} \qquad (6)$$

where C_{spin} is the concentration of the free radical in the protein sample, $C_{standard}$ is the concentration of the spin standard, $\iint I_{spin}$ and $\iint I_{standard}$ are the spectroscopic intensities of the sample and the spin standard respectively, obtained by taking a double integral for their EPR spectra, H_{mod} is the field modulation, T is the temperature, and P is the microwave power.

The yield of the free radical protein can be calculated by:

$$Yield = \frac{C_{spin}}{C_{protein}} \qquad (7)$$

where $C_{protein}$ is the concentration of the total protein.

Based on this equation, the concentration of the free radical in our 1.3mM unlabeled Tyr-Cys· oxidized apoGAOX is 0.22mM and the yield is 17%.

2.6 *Field/Frequency Calibration Standard Preparation*

Free radical diphenylpicrylhydrazyl (DPPH) with g_{DPPH} = 2.0036 ± 0.0003 (12) was prepared in a Microbore tubing with 0.040in interior diameter for field/frequency calibration. One end of the tubing was sealed with Instant Krazy Glue® and the open end of the tubing was connected to the tip of the small glass pipette. After the glue had cured, DPPH powder was added to the tubing through the pipette. The open end of the tubing was then sealed with Instant Krazy Glue®.

2.7 *Spectroscopic Measurements*

X-band (9.2-9.9GHz) EPR spectra were recorded using a Bruker Elexsys E500 spectrometer equipped with a Bruker ER049X SuperX X-Band microwave bridge, Bruker ER4122SHQE super high Q high sensitivity cavity, and a E27H lock-in detector. Temperature control was provided by a continuous nitrogen flow cryostat system, in which the temperature was monitored with Bruker W1100321 thermocouple probe. The EPR spectra were displayed and analyzed using the Bruker XeprView interface. The EPR spectrometer and cryostat system were stabilized for 2-3 hours before collecting the data. Power saturation measurements of unlabeled Tyr-Cys· oxidized apoGAOX were performed at 100K with 1G modulation amplitude. The 9.396GHz spectra were collected over a microwave power range (0.2μW-200mW, 60dB-0dB) and calibrated with DPPH field/frequency spin standard using published g-value (g_{DPPH} = 2.0036). The spectroscopic intensities were recorded for further analysis. First harmonic X-band EPR spectra of the deuterium-labeled, ^{13}C-labeled, ^{33}S-labeled and ^{17}O-labeled samples were collected at ~50μW (36dB) and ~20mW (10dB). In all the experiments, first harmonic spectra of free radical DPPH were collected for field/frequency calibration at ~50μW (36dB) and ~20mW (10dB) immediately before and after collecting the spectra of the

protein samples. A duplicate set of EPR spectra was collected for each sample to confirm the accuracy of the data.

2.8 EPR Data Analysis

2.8.1 Power Saturation

In Bruker XeprView interface, baseline correction was applied to the spectra of the power saturation measurements. The spectral data then imported in Specfit 3.0 global fitting data analysis software, and analyzed using the Model-free Evolving Factor Analysis (EFA) routine. This method factor-analyzes the spectra and resolves component spectra (basis vectors) from the entire data set. The two spectral components extracted by EFA together with the spectroscopic intensities recorded during the power saturation experiment were imported into the graphing program Kaleidagraph for further analysis. The power dependence of the two components was fit using least-squares methods (21) to an equation of a form:

$$log\,(I / \sqrt{P}) = -(b_i/2)\,log\,(P_{½} + P) + (b_i/2)\,log\,(P_{½}) + log\,k_i$$

$$= log\left(\frac{P_{1/2} \times k_i^{2/b_i}}{P_{1/2} + P}\right)^{b_i/2} \qquad (8)$$

where I is the signal intensities, $P_{½}$ is the microwave power required for half saturation, P is the microwave power, b_i (i = 1, 2) is the inhomogeneity factor, and k_i (i = 1, 2) is the proportionality factor for the ith component.

The recorded spectroscopic intensities of the raw data were also fit using least-squares methods. Since the raw data combines the data of the two components, an additional term is required:

$$log\,(I / \sqrt{P}) = log\left[\left(\frac{P_{1/2} \times k_i^{2/b_i}}{P_{1/2} + P}\right)^{b_i/2} + \left(\frac{P'_{1/2} \times k_i^{2/b_i}}{P'_{1/2} + P}\right)^{b_i/2}\right] \qquad (9)$$

where $P_{½}$ and $P'_{½}$ are the parameters of the low and high power components respectively. A plot of *log* (I / $\sqrt{P}$) vs. microwave power was obtained and the values of $P_{½}$, b_i and k_i were determined from the fittings.

2.8.2 Baseline and Field Corrections

Spectrum simulation by a continuous wave (CW) EPR computer simulation software suite XSophe 1.1.4 was performed for the spectra from protein samples to extract detailed structural information, such as g-values, and hyperfine coupling constants. Baseline and field (ΔH_{corr}) corrections were applied to the experimental spectra in Bruker XeprView interface before performing simulation in XSophe. The field correction was calculated by comparing the known g-value of DPPH (g_{DPPH} = 2.0036) with the observed g-value.

$$\Delta H_{corr} = 0.71448 \times (\nu / g_{DPPH}) - H_{obs} = H' - H_{obs} \quad (10)$$

where ν is the frequency in MHz of the experimental spectrum of DPPH, g_{DPPH} is the literature g-value of DPPH and H_{obs} is the observed crossing point in G. H' is the predicted crossing point calculated using the literature g-value of DPPH. ΔH_{corr} was applied to the spectra as an X-shift based on the number of data points (n).

$$\text{X-shift} = \Delta H_{corr} \times n / sw \quad (11)$$

where n = 1024 and sw is the sweep width.

2.8.3 XSophe Simulation

EPR spectra may be very complex, but they can be fundamentally described in terms of a spin Hamiltonian (22). For a paramagnetic system (S = ½) with anisotropic g-values and hyperfine coupling constants, the general spin Hamiltonian (H_{sp}) is:

$$H_{sp} = \beta B \cdot \boldsymbol{g} \cdot S + \sum S \cdot \boldsymbol{A} \cdot I \quad (12)$$

where S is the electron spin operator, I is the nuclear spin operator, $\boldsymbol{g}$ is the electron Zeeman matrix, $\boldsymbol{A}$ is the hyperfine coupling matrix, β is the Bohr magneton, and B is the applied magnetic field.

In XSophe, the EPR spectrum was calculated by integrating over spherical angles to simulate the orientation averaged spectrum of a randomly orientated powder sample using the following integration:

$$S(B,\nu_c) = \sum_{i=0}^{N} \sum_{j=i+1}^{N} C \int_{\theta=0}^{\pi} \int_{\phi=0}^{\pi} |\mu_{ij}|^2 f[\nu_c - \nu_o(B), \sigma_\nu] d\cos\theta d\phi \qquad (13)$$

where $S(B, vc)$ denotes the spectral intensity, $|\mu_{ij}|^2$ represents the i→j transition, v_c is the microwave frequency, $v_o(B)$ is the resonant frequency, σ_v is the spectral line width, $f[v_c - v_o(B), \sigma_v]$ is the spectral line shape function (Gaussian or Lorentzian), θ and ϕ are the polar and azimuthal angles respectively and C is the normalization constant.

2.8.4 Simulation Procedures

Full Matrix Diagonalization methods were generally used for the simulations (Figure 2.1). In X-windows graphical user interface provided by XSophe, electron spin center and its nearby nuclei along with their isotope abundance were defined based on the structure of free radical protein sample. The spin Hamiltonian interactions and their initial spin Hamiltonian parameters (g-values, hyperfine coupling constants, and line widths) together with the limits (deviations, and parameter half-spaces) were set up for the simulation. Simplex Optimization method and Peak Extrema Normalization method were used. All the simulations underwent iterative optimization. The results were further refined by minor manual adjustments of the parameters and the limits. The values for the parameters (g tensors, hyperfine coupling constants, and line widths) were evaluated from the simulated spectrum.

2.8.5 Error Estimation of g-values

Error (σ) estimation was a crucial process to confirm the accuracy of the spectral g-values obtained from XSophe simulation. The error (σ) of each parameter (g_x, g_y or g_z) was determined individually by XSophe simulation. For example, g_x was varied systemically (+0.0001 intervals) with g_y and g_z unchanged to obtain a set of simulated

spectra. The error (ε_i) for the simulated spectrum at each particular g_i value could be determined by:

$$\varepsilon_i = \sum_{j=1}^{n} \frac{[E - S(g_i)]^2}{E^2} \tag{14}$$

where *i* represents the three principal components x, y and z, n is the number of data points for each spectrum, *E* is the experimental spectrum, and $S(g_i)$ is the simulated spectrum at each particular g_i value. The denominator E^2 is a normalization constant. After obtaining the errors (ε_i) for each spectrum, the g_x value (g_{min}) with the minimum error (ε_{min}) could be observed from a plot of Errors (ε) vs. g_x (Figure 2.2). The width (2σ) of the curvature was obtained as the difference between the two g-values which possessed $2\varepsilon_{min}$. The value of g_x could then be represented as $g_{min} \pm \sigma$. The same procedure was repeated for g_y and g_z.

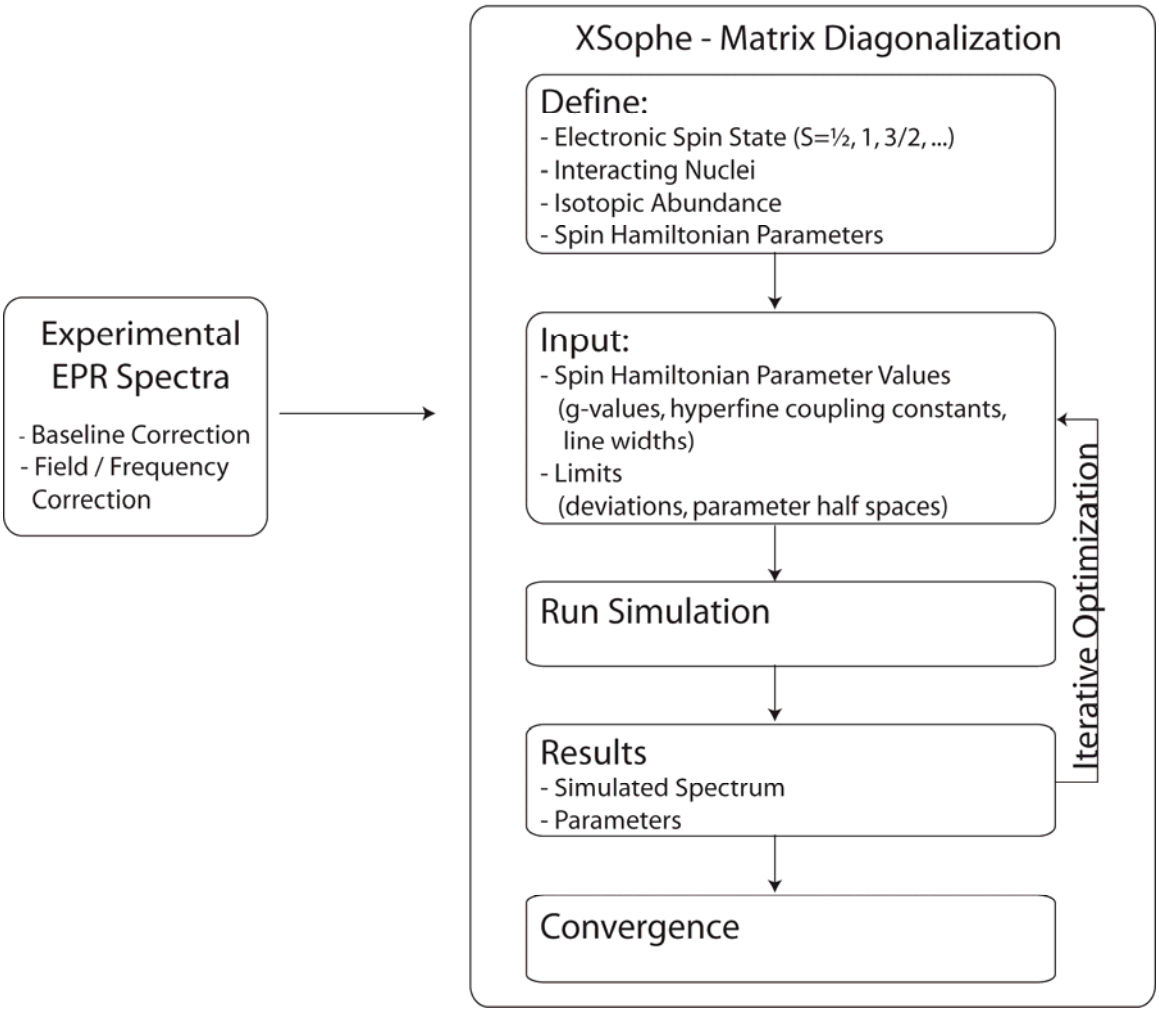

Figure 2.1 Flow Chart of the progress of XSophe Simulation.

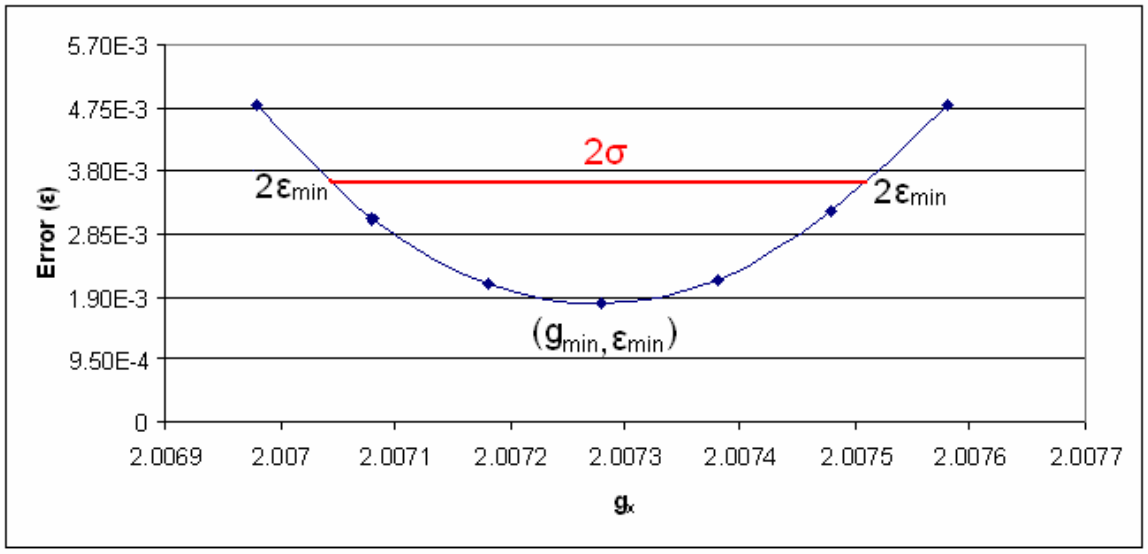

Figure 2.2 Error estimation plot for g_x. The minimum error is found at g_{min}. The red solid line represents the width (2σ) of the curvature between the two g-values, which possess $2\varepsilon_{min}$.

CHAPTER 3
RESULTS

3.1 *Power Saturation Analysis*

Power saturation measurements of unlabeled Tyr-Cys· oxidized apoGAOX were performed at microwave powers 0.2μW-200mW (60dB-0dB). The spectra were shown in a 3-D plot in Figure 3.1a. Experimental spectra from these measurements were analyzed with Model-free EFA to extract two spectra that corresponded to the two different components in the sample (3.1b). A plot of $log(I / \sqrt{P})$ vs. microwave power for the two spectra extracted from EFA calculation and the experimental data from the power saturation measurements is shown in Figure 3.1b. The low and high power components matched the low power region (P<100μW) and high power region (P>10mW) of the experimental data respectively, confirming two components, saturating at different microwave powers, were present in the sample. Moreover, the experimental data was fit with Equation (9), which contained two terms that represented the high and low power components (solid red line shown in Figure 3.1c).

Based on the least-square fitting with Equation (8) for the EFA data, $P_{½}$ for the low and high power species were 86μW (34dB) and 4055μW (16dB) respectively. These values provided a basic guideline for choosing the best operational power for GAOX samples. After reviewing all the spectra collected at different power levels, the spectrum at 50μW (36dB) was chosen as the best operational power for the samples.

Even though the least-square fit showed that the high power species began its saturation at 4055μW, a higher microwave power level (20mW) was chosen for collecting the spectra of the high power components. Because the low power component would be completely saturated at such a high power, so the EPR signal obtained would purely come from the high power component. In addition to the $P_{½}$ values, the least-square fit also provided us with the values of the inhomogeneity factors and proportionality factors, so two simulated curves ranging from 0.1μW to 10^6μW for the low and high power components could be formulated. From the simulated curves, it showed that the high power component would not start its saturation before 1000μW, so the EPR spectra collected at microwave power lower than 1000μW would all contain the high power component. The signal intensity of the high power component at low power was $10^{5.1}$ while the signal intensity of the low power component at low power was $10^{6.2}$. Therefore, the EPR spectrum collected at low power contained about 7% of the high power component. When the microwave power increased, the low power component, which was the Tyr-Cys phenoxyl free radical, would saturate, leaving only the high power component, which might be another tyrosine derived free radical. Therefore, the EPR signal would be dominated by the contribution of the high power component. However, 7% of the 17% yield was actually very small, so the high power species was actually a minor component in our sample and we chose not to investigate it further.

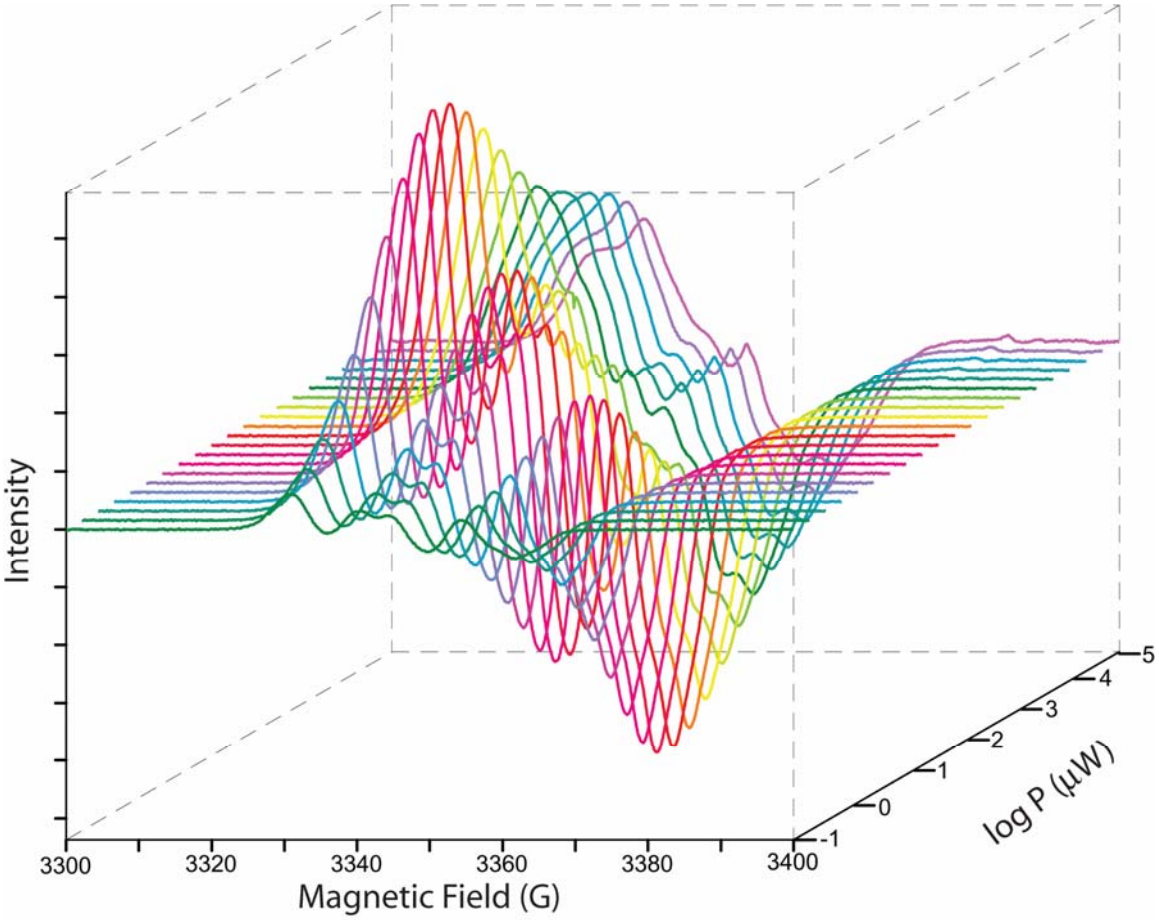

Figure 3.1a EPR spectra of unlabeled Tyr-Cys· oxidized apoGAOX collected at 0.2μW-200mW (60dB-0dB).

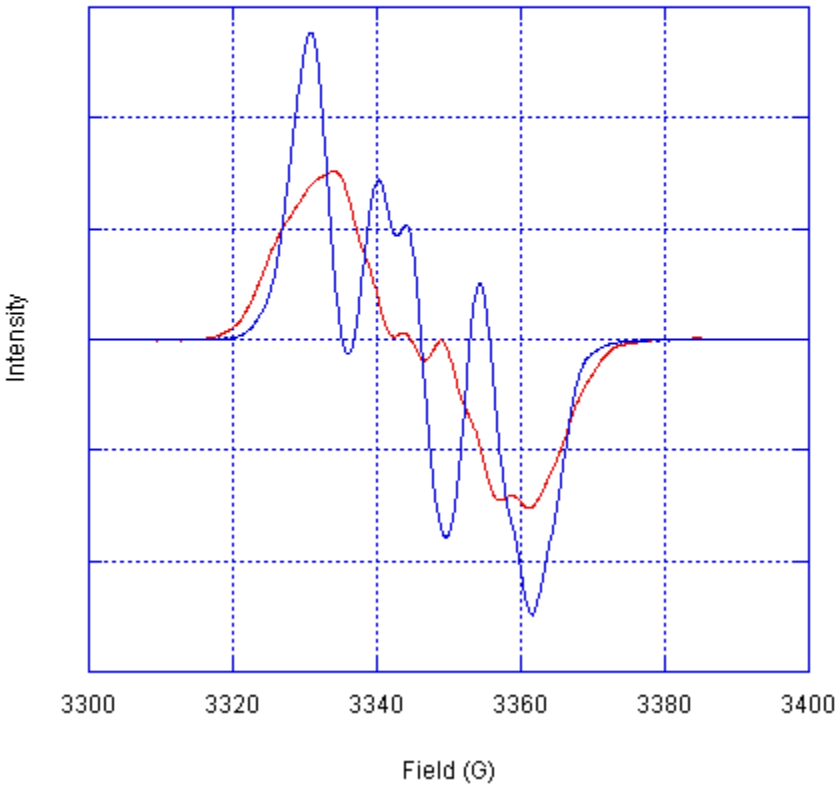

Figure 3.1b Two unique spectra extracted by EFA method. The low power component is shown in blue and the high power component is shown in red.

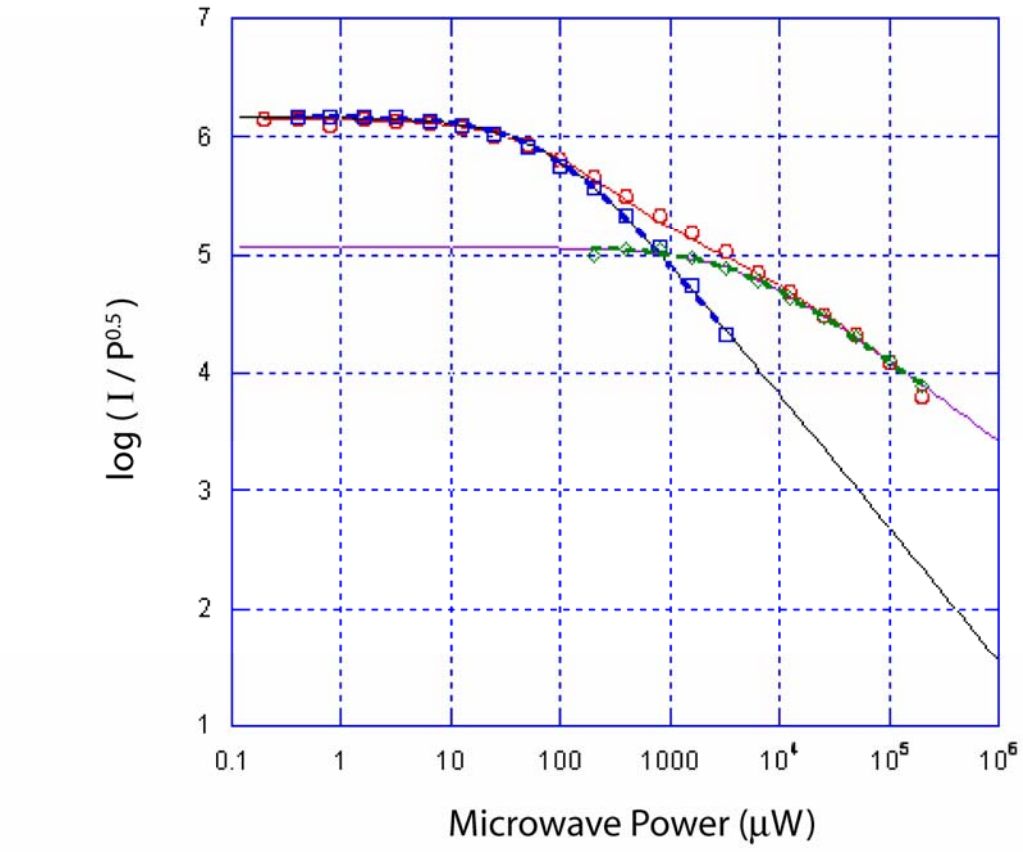

Figure 3.1c Power saturation plot of unlabeled Tyr-Cys· oxidized apoGAOX. The experimental data (○) recorded from the power saturation measurements, and the data for the low (□) and high (◊) power components extracted from EFA calculation are shown. The solid red line is the least-square fit of the experimental data using Equation (9). The blue and green dash lines are the least-square fit of the low and high power components respectively using Equation (8). The black and purple solid lines are the simulated curves of low and high power components respectively using the parameters obtained from least-square fit.

3.2 XSophe Simulation

3.2.1 Isotope Derivatives of GAOX

EPR spectra were collected for ten different isotope derivatives of GAOX (Figure 3.2) at 50μW (36dB) and 20mW (10dB). These isotope derivatives may be divided into four groups – ^{2}H-labeled, ^{13}C-labeled, ^{17}O-labeled, and ^{33}S-labeled. For the ^{2}H-isotope labeled samples, β, β'-d_2 Tyr (Figure 3.2b) contained two ^{2}H on C7 while the β, β'-H_2 Tyr (Figure 3.2c) contained three ^{2}H on C2, C5, and C6. 2,6-d_2 Tyr (Figure 3.2d) contained ^{2}H on C2 and C6 while 3,5-d_2 Tyr (Figure 3.2e) contained ^{2}H on C5 with the ^{2}H on C3 replaced by a Cys residue. All of the protons were replaced by ^{2}H for the perdeuterated Tyr (Figure 3.2f) oxidized apoGAOX. Three of the protein samples are ^{13}C-labeled. Phenol-4-^{13}C Tyr (Figure 3.2g) had its ^{13}C at C4 while phenol-3,5-$^{13}C_2$ (Figure 3.2h) had its ^{13}C at C3 and C5. All of the ring carbon atoms of $^{13}C_6$ ring Tyr (Figure 3.2i) were substituted with ^{13}C. In addition, ^{16}O on C4 was replaced by ^{17}O (Figure 3.2j) and ^{32}S of Cys was substituted with ^{33}S (Figure 3.2k) for the isotope labeled samples. Since the isotopes possessed non-zero nuclear spin (*I*), the interaction between the free radical and the nearby nuclei gave rise to additional hyperfine coupling. In principle, determination of those hyperfine coupling constants by XSophe simulation can help map out the unpaired electron spin density distribution on Tyr-Cys amino acid and therefore experimentally define the electronic structure of the free radical site of GAOX.

3.2.2 Unlabeled Tyr-Cys· oxidized apoGAOX

Unlabeled Tyr-Cys· oxidized apoGAOX basically consisted of a doublet of doublet structure since the major hyperfine coupling came from the interaction between the free radical in the ring and the methylene protons with spectral width of ~58G. EPR spectra of this unlabeled sample are shown in Figure 3.3 for comparison with other labeled samples.

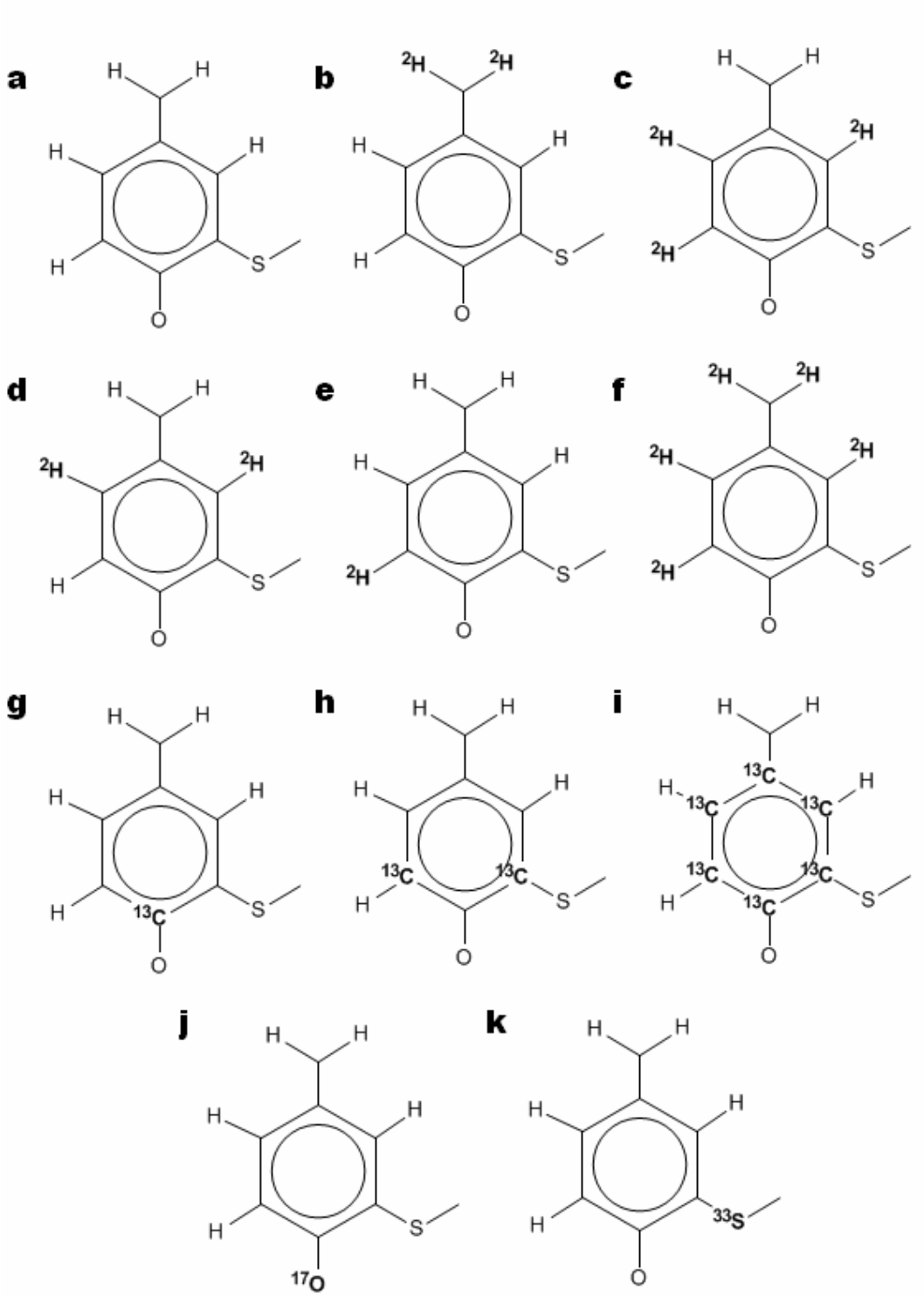

Figure 3.2 Structures of unlabeled and labeled Tyr-Cys amino acids. **a)** unlabeled **b)** β, β'-d_2 **c)** β, β'-H_2 **d)** 2,6-d_2 **e)** 3,5-d_2 **f)** perdeuterated **g)** phenol-4-^{13}C **h)** phenol-3,5-$^{13}C_2$ **i)** $^{13}C_6$ Ring **j)** ^{17}O **k)** ^{33}S

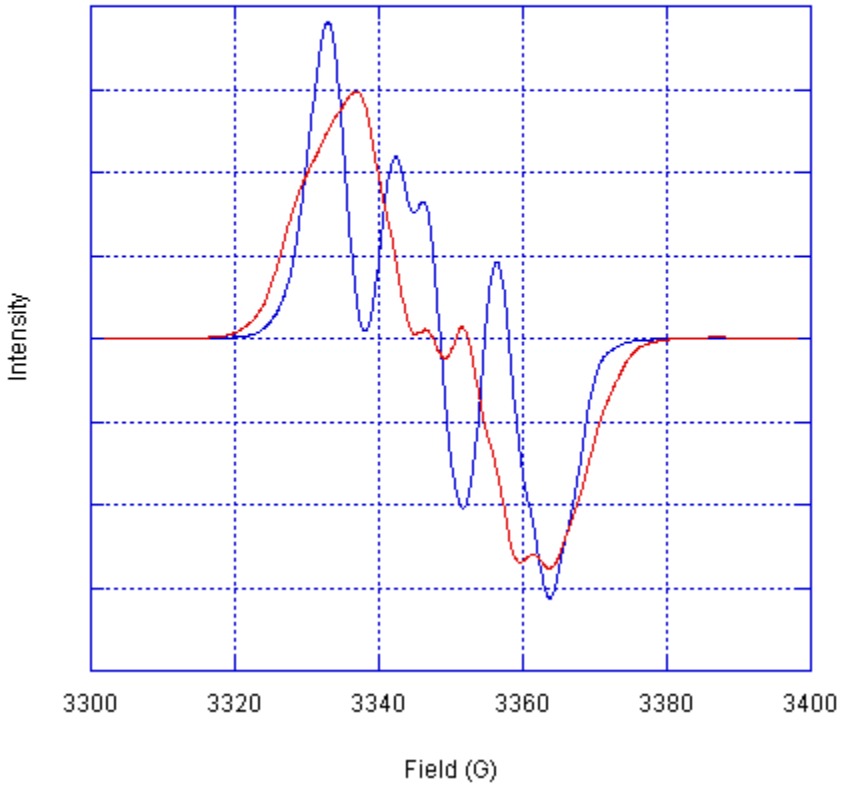

Figure 3.3 EPR Spectra of unlabeled Tyr-Cys· oxidized apoGAOX. The low power spectrum is shown in blue (50μW) and the high power spectrum is shown in red (20mW).

3.2.3 Perdeuterated Tyr-Cys· oxidized apoGAOX

XSophe simulation was first performed for perdeuterated Tyr-Cys· oxidized apoGAOX (Figure 3.2f) after a ΔH_{corr} of +1.79G was applied to the EPR spectrum in order to determine the g anisotropy of the sample. Since all of the protons were replaced by ^{2}H in perdeuterated Tyr-Cys· sample, the small magnetic moment of ^{2}H gave rise to a smaller contribution of hyperfine coupling to the EPR spectrum. Therefore, g-anisotropy dominates over the hyperfine coupling. Moreover, perdeuterated Tyr-Cys· sample gave a simple singlet derivative structure with narrow linewidths and spectral width (~42G), so the linewidths would not be a factor that distorted the EPR spectrum and affected the accuracy of the g values obtained from the simulation. The spectrum was simulated as a second harmonic spectrum in order to obtain the best quality of fit because the second derivative spectrum possessed more resolved features. The simulation was set up for a ^{12}C with anisotropic g-values. The small ^{2}H hyperfine coupling constants were ignored for this simulation, and included in the linewidth term. The simulated spectrum and the two experimental spectra are shown in Figure 3.4a. It showed that the two experimental spectra were the same after applying the frequency correction to the second spectrum. This confirmed the accuracy of the spectra that we obtained. The simulated spectrum was very close to the experimental spectra, giving rise to a set of spectral parameters (Table 3.1). Using those parameters in the first harmonic simulation for perdeuterated Tyr-Cys· sample also gave a very good fit (Figure 3.4b).

Table 3.1 Spectral parameter values for perdeuterated Tyr-Cys· oxidized apoGAOX at 50μW.

	g	Linewidth (G)
x	2.00756	3.56
y	2.00655	3.55
z	2.00219	3.47

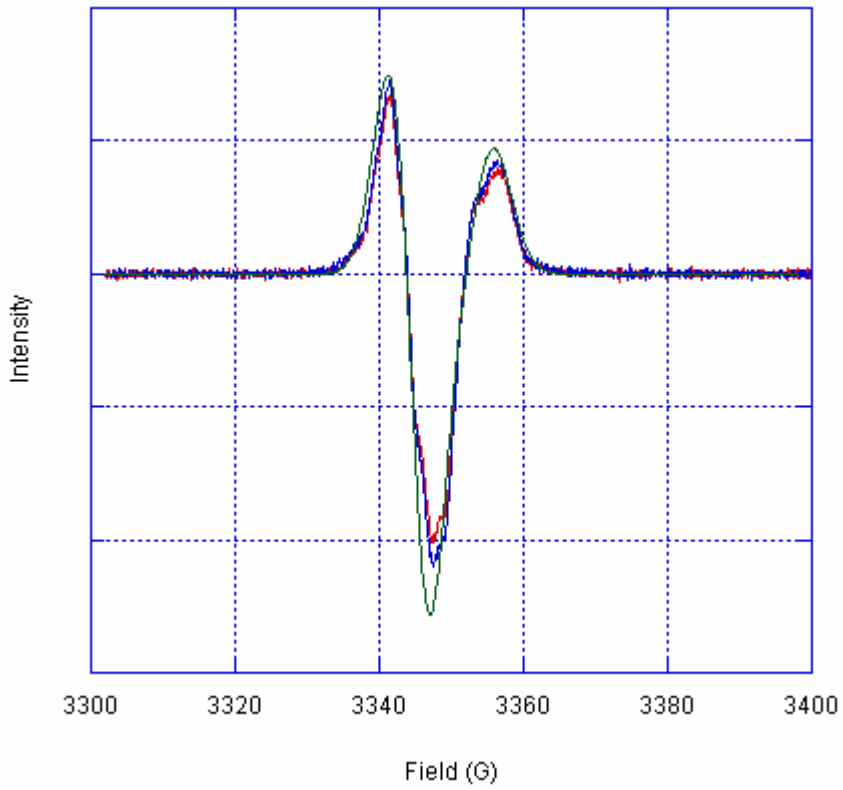

Figure 3.4a Second Derivative EPR Spectra of perdeuterated Tyr-Cys· oxidized apoGAOX. The red solid line is the first experimental spectrum. The blue solid line is the second experimental spectrum and the green solid line is the XSophe simulated spectrum.

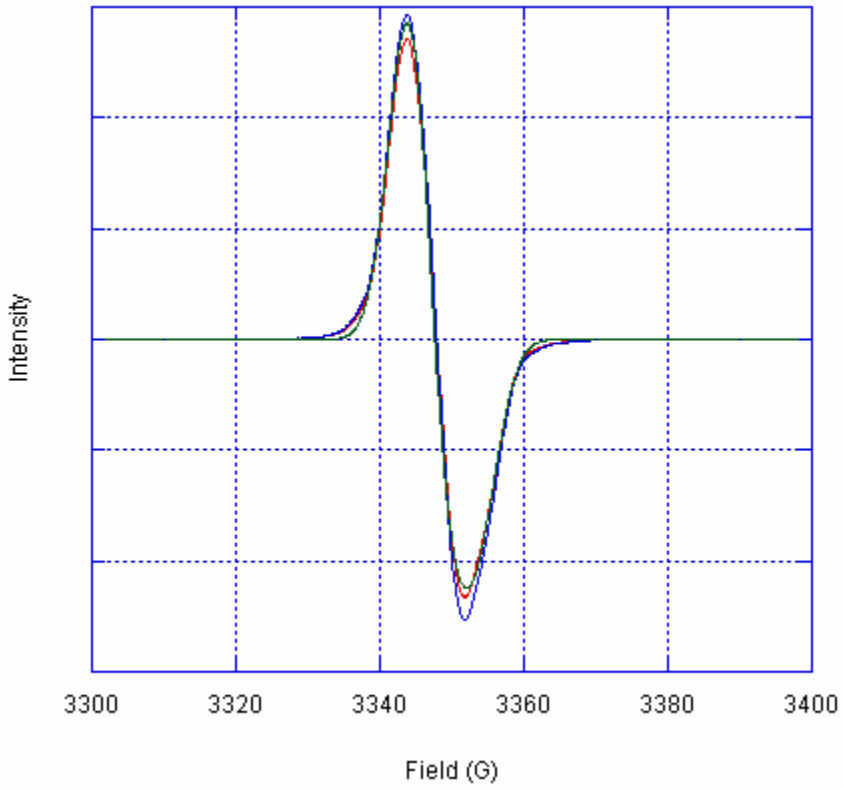

Figure 3.4b First Derivative EPR Spectra of perdeuterated Tyr-Cys· oxidized apoGAOX. The red solid line is the first experimental spectrum. The blue solid line is the second experimental spectrum and the green solid line is the XSophe simulated spectrum.

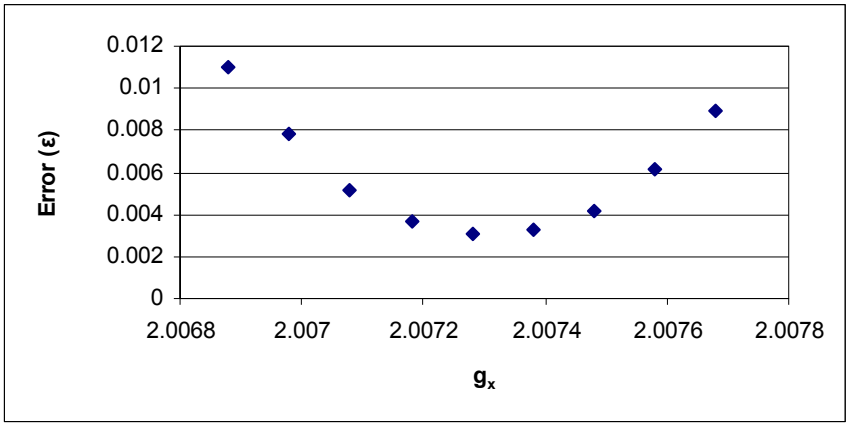

Figure 3.5a Error estimation plot for g_x of perdeuterated perdeuterated Tyr-Cys· oxidized apoGAOX.

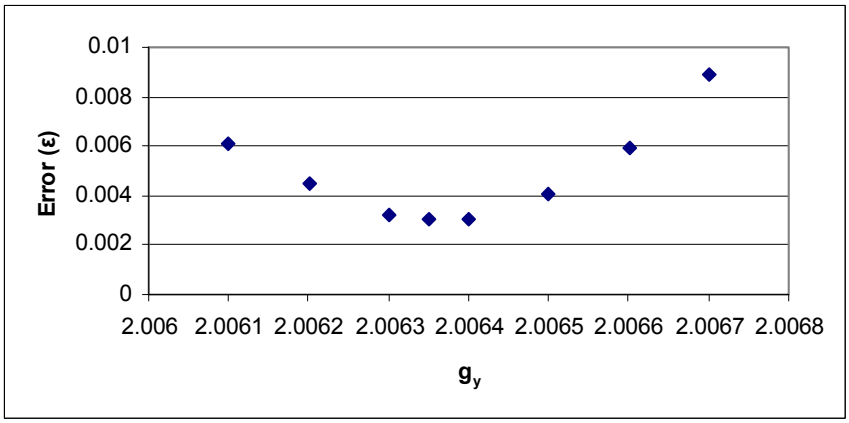

Figure 3.5b Error estimation plot for g_y of perdeuterated perdeuterated Tyr-Cys· oxidized apoGAOX.

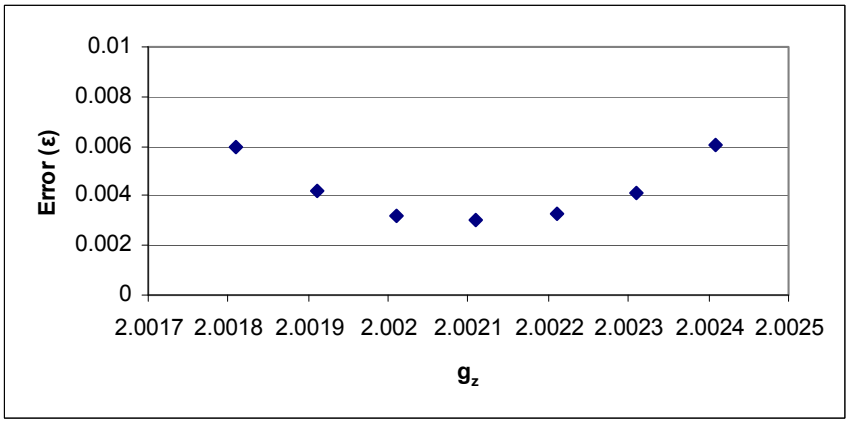

Figure 3.5c Error estimation plot for g_z of perdeuterated perdeuterated Tyr-Cys· oxidized apoGAOX.

The errors of the g-values were determined from the Figure 3.5. For g_x, the minimum error (ε_{min} = 0.00309) was found at g_x = 2.00728. 2σ could be estimated as 0.0006 from g_x = 2.00703 and 2.00758. Therefore, g_x = 2.00728 ± 0.00030. For g_y, the minimum error (ε_{min} = 0.00304) was found at g_y = 2.00635. 2σ could be estimated as 0.0005 from g_y = 2.00610 and 2.00662. Therefore, g_y = 2.00635 ± 0.00025. For g_z, the minimum error (ε_{min} = 0.00302) was found at g_z = 2.00211. 2σ could be estimated as 0.0006 from g_z = 2.00181 and 2.00241. Therefore, g_z = 2.00211 ± 0.0003.

XSophe simulation was also performed for EPR spectrum of perdeuterated Tyr-Cys· oxidized apoGAOX collected at high power (20mW) after a ΔH_{corr} of +1.98G was applied to the EPR spectrum. This high power spectrum possessed an asymmetric derivative shape with shoulders at the low and high field sides. The generation of this unique feature was due to the increase contribution of the high power component to the EPR signal while the low power component was saturating. The simulated spectrum and the two experimental spectra are shown in Figure 3.6. It showed that the two experimental spectra were the same after applying the frequency correction to the second spectrum. The simulated spectrum was very close to the experimental spectra, giving rise to a set of spectral parameters (Table 3.2).

Table 3.2 Spectral parameter values for perdeuterated Tyr-Cys· oxidized apoGAOX at 20mW.

	g	Linewidth (G)
x	2.00830	4.92
y	2.00520	3.64
z	2.00163	4.96

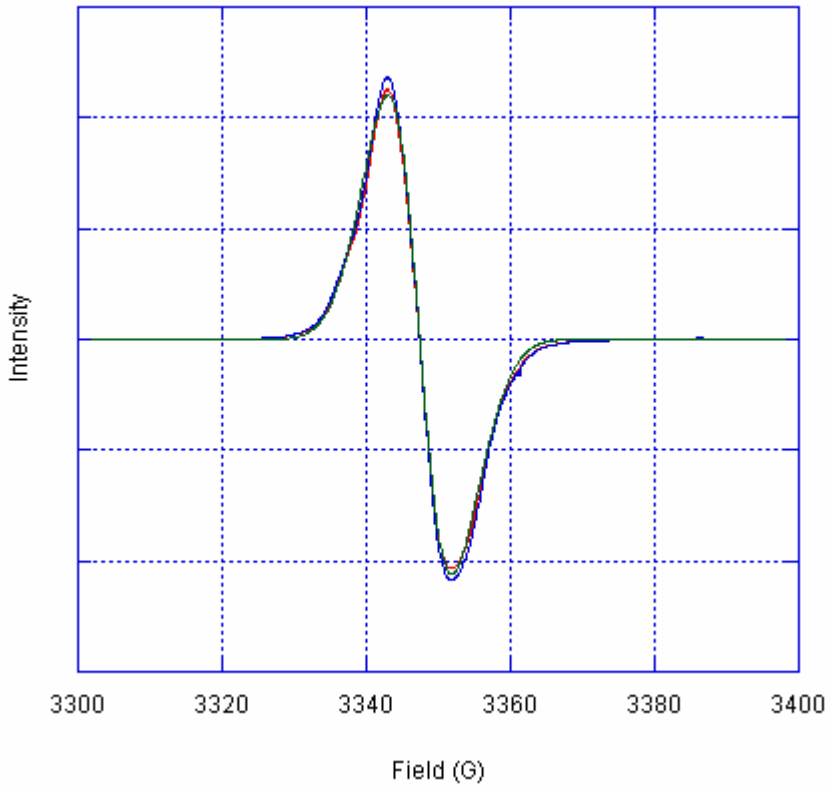

Figure 3.6 First Derivative EPR Spectra of perdeuterated Tyr-Cys· oxidized apoGAOX at 20mW (10dB). The red solid line is the first experimental spectrum. The blue solid line is the second experimental spectrum and the green solid line is the XSophe simulated spectrum.

3.2.4 β, β'-H_2 Tyr-Cys· oxidized apoGAOX

In oxidized apoGAOX, the principal contribution to the hyperfine interaction has been assigned to the two methylene protons because of the overlapping orbitals of C1 and H_β. Therefore, XSophe simulation was performed for β, β'-H_2 Tyr-Cys· oxidized apoGAOX (Figure 3.2c) after a ΔH_{corr} of +2.02G was applied to the EPR spectrum in order to determine the hyperfine coupling constants of the two methylene hydrogen. With all the ring protons substituted with ^{2}H, the EPR spectrum of this sample was very similar with the spectrum of unlabeled sample with spectral width of ~64G. Because the contribution from the ring protons was relatively small when compared to the methylene protons, the substitution would not cause a dramatic change on the EPR spectrum. The simulation was set up for a ^{12}C with anisotropic g-values and two anisotropic hyperfine coupling constants for the two protons at the β position. Using the g-values obtained from the simulation of perdeuterated Tyr-Cys· sample, the XSophe simulation was simplified to only contain two major sets of unknown parameter- the hyperfine coupling constants for the methylene protons. Initial values for the simulation were based on values obtained by Gerfen (23) and refined those parameter values by manually adjusting them to obtain the best result. The simulated spectrum and the two experimental spectra are shown in Figure 3.7. After applying the frequency correction to the second spectrum, it superimposed on the first spectrum, demonstrating the reliability of the spectra. The simulation was able to reproduce the essential features of the experimental spectra, providing estimates of the spectral parameters (Table 3.3). The hyperfine coupling constants of the methylene protons obtained in this analysis could then be used in the simulations for the rest of the samples.

Table 3.3 Spectral parameter values for β, β'-H_2 Tyr-Cys· oxidized apoGAOX at 50μW.

	g	$A_{\beta1}$ (G)	$A_{\beta2}$ (G)	Linewidth (G)
x	2.00700	14.75	9.00	1.87
y	2.00655	14.68	9.57	2.17
z	2.00224	14.30	8.11	1.57

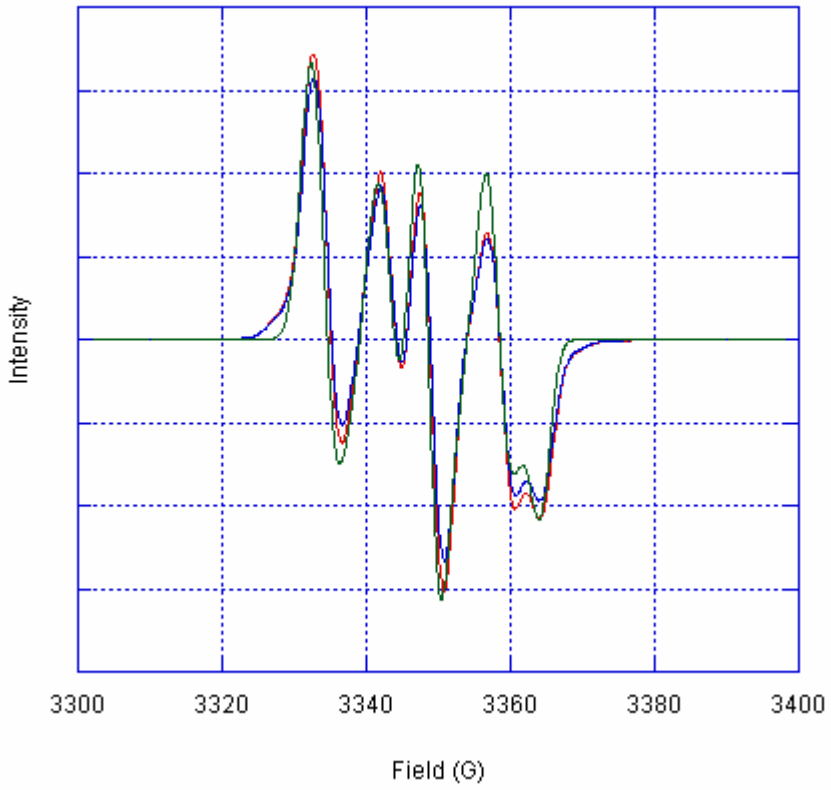

Figure 3.7 EPR Spectra of β, β'-H_2 Tyr-Cys· oxidized apoGAOX. The red solid line is the first experimental spectrum. The blue solid line is the second experimental spectrum and the green solid line is the XSophe simulated spectrum.

To illustrate the effect of the β hyperfine interaction, we performed a simulation for the low power EPR spectrum of perdeuterated Tyr-Cys· sample again without hyperfine coupling constants, but with very narrow linewidths. From Figure 3.8a, the simulation gave a very resolved spectrum with narrow linewidths and the peaks represented the g-values we input. If we divided the hyperfine coupling constants determined from the result of β, β'-H_2 Tyr-Cys· oxidized apoGAOX by a factor of 6.5 and transferred them to the simulation, the simulated spectrum matched the experimental spectrum perfectly (Figure 3.8b), giving rise to a new set of parameter values (Table 3.4).

Table 3.4 Spectral parameter values for perdeuterated Tyr-Cys· oxidized apoGAOX with hyperfine coupling constants.

	g	$A_{\beta 1}$ (G)	$A_{\beta 2}$ (G)	Linewidth (G)
x	2.00741	2.26	1.38	1.57
y	2.00641	2.26	1.38	1.57
z	2.00215	2.26	1.38	1.57

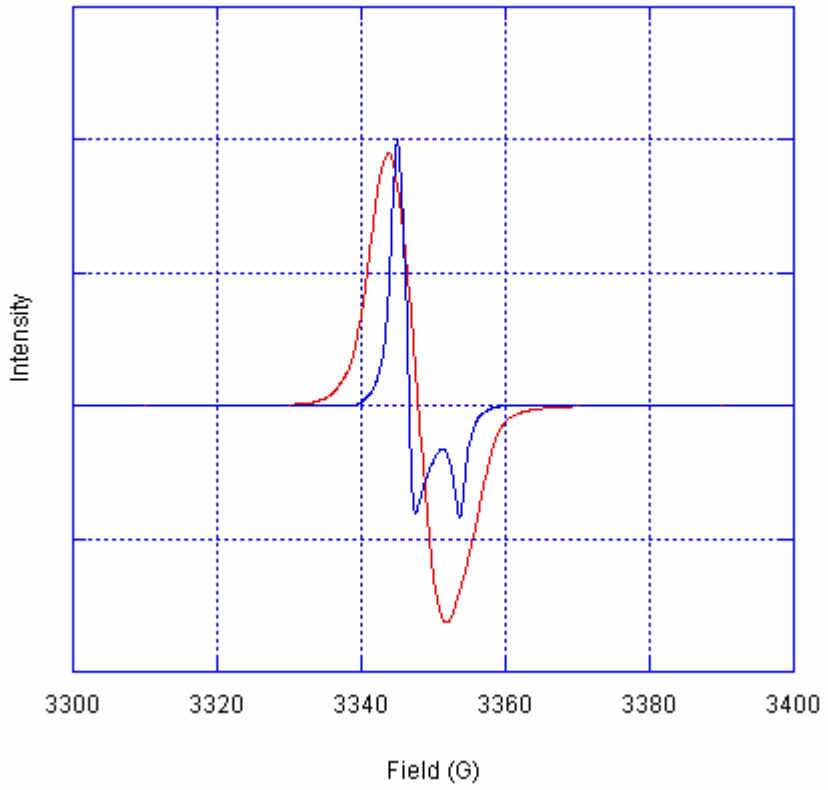

Figure 3.8a EPR Spectra of perdeuterated Tyr-Cys· oxidized apoGAOX *without* hyperfine coupling constants, but with very narrow linewidths. The red solid line is the experimental spectrum. The blue solid line is the XSophe simulated spectrum.

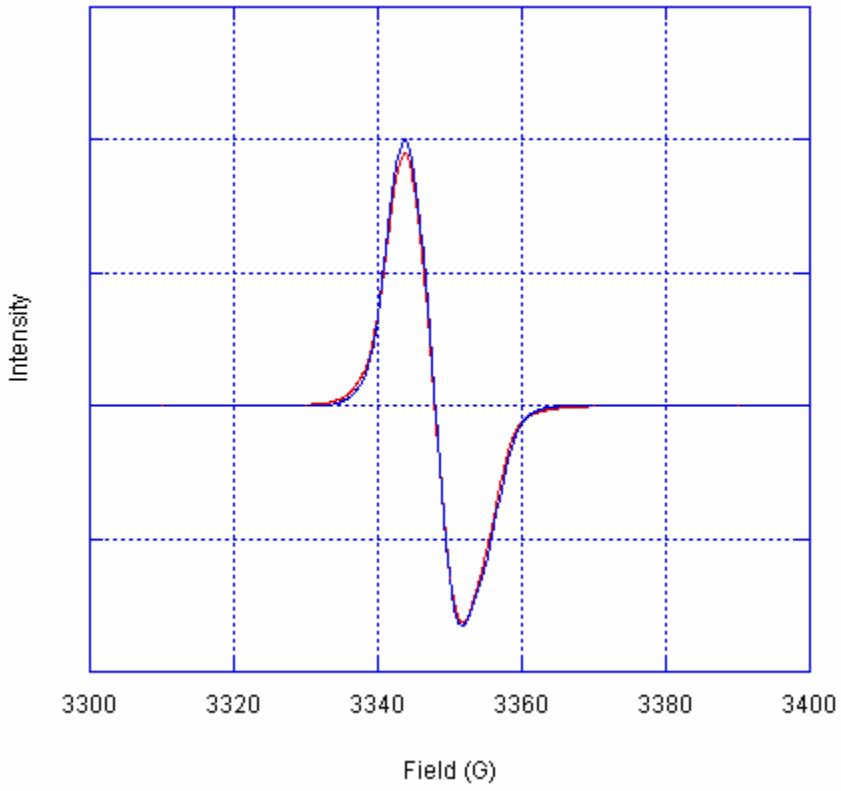

Figure 3.8b EPR Spectra of perdeuterated Tyr-Cys· oxidized apoGAOX *with* hyperfine coupling constants. The red solid line is the experimental spectrum. The blue solid line is the XSophe simulated spectrum.

Using the program created by Svistunenko and Cooper (25), we could calculate the rotation angle (θ) of the phenoxyl ring to the methylene protons around the C1-C7 bond from the experimentally determined hyperfine coupling constants of H_β by two equations:

$$A^{\beta 1}_{iso} = \rho_{C1} B'' \cos^2\theta \quad (15)$$

$$A^{\beta 2}_{iso} = \rho_{C1} B'' \cos^2(\theta - 120°) \quad (16)$$

where $A^{\beta 1}_{iso}$ and $A^{\beta 2}_{iso}$ represented the isotropic hyperfine coupling constants of the two methylene protons, ρ_{C1} was the electron spin density on C1 and B'' is a constant, being equal to 58G (25). The definition of the rotation angle was shown in Figure 3.9.

From the simulation of β, β'-H_2 Tyr-Cys· oxidized apoGAOX, the anisotropic hyperfine coupling constants of the two methylene protons was determined (Table 3.3). The average of the three anisotropic hyperfine coupling constants ($A^{\beta 1}_{iso}$ = 14.58G and $A^{\beta 2}_{iso}$ = 8.89G) was used to calculate the rotation angle. Four solutions (Figure 3.10) were obtained in this calculation with two of them possessed the same $\rho_{C1} B''$ value and the other two contained another value of $\rho_{C1} B''$. The two rotation angles corresponding to ρ_{C1} = 16.1G / 58G = 0.278 were -18.0° and -42.0° while the other two rotation angles corresponding to ρ_{C1} = 46.5G / 58G = 0.802 were 55.9° and 61.4°.

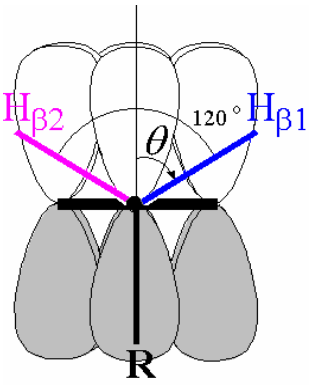

Figure 3.9 Definition of the rotation angle of the phenoxyl ring to the methylene protons around the C1-C7 bond (25).

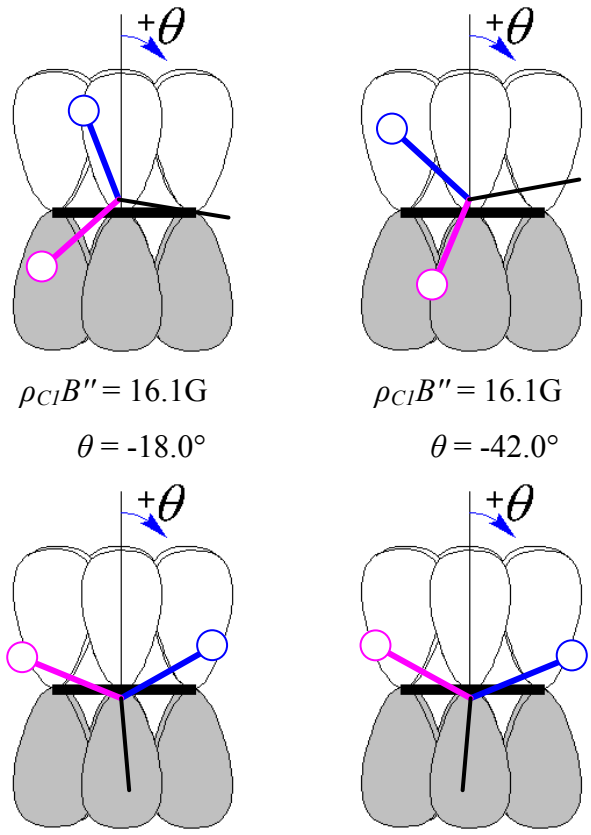

$\rho_{C1}B'' = 16.1\text{G}$ $\theta = -18.0°$

$\rho_{C1}B'' = 16.1\text{G}$ $\theta = -42.0°$

$\rho_{C1}B'' = 46.5\text{G}$ $\theta = 55.9°$

$\rho_{C1}B'' = 46.5\text{G}$ $\theta = 64.1°$

Figure 3.10 Four solutions of the rotation angles of the phenoxyl ring to the methylene protons around the C1-C7 bond.

3.2.5 β, β'-d_2 Tyr-Cys· oxidized apoGAOX

For β, β'-d_2 Tyr-Cys· oxidized apoGAOX (Figure 3.2b), the two β positions were occupied by two ^{2}H, diminishing the hyperfine coupling interaction. In addition, the hyperfine coupling interaction from the ring protons was not strong enough to give a splitting. Therefore, β, β'-d_2 Tyr-Cys· oxidized apoGAOX could only give rise to a simple singlet derivative structure with spectral width of ~46G. The EPR spectrum for this sample was more spread out with a larger linewidth when compared to perdeuterated Tyr-Cys· oxidized apoGAOX. This broadening is likely due to the unresolved interaction with the three ring protons. First harmonic XSophe simulation was performed after a ΔH_{corr} of +2.18G was applied to the EPR spectrum. The simulation was set up for a ^{12}C with anisotropic g-values, and two isotropic hyperfine coupling constants for the two methylene ^{2}H. The hyperfine coupling constants of the methylene ^{2}H obtained from the previous analysis could be transferred to this simulation. The simulated spectrum and the two experimental spectra are shown in Figure 3.11. The second experimental spectrum superimposed on the first spectrum after the frequency correction. The simulated spectrum showed the same singlet structure as the experimental spectrum with all the turning points at the same position, giving rise to a set of spectral parameters (Table 3.5).

Table 3.5 Spectral parameter values for β, β'-d_2 Tyr-Cys· oxidized apoGAOX at 50μW.

	g	$A_{\beta1}$ (G)	$A_{\beta2}$ (G)	Linewidth (G)
x	2.00740	2.26	1.38	2.65
y	2.00640	2.26	1.38	2.65
z	2.00211	2.26	1.38	2.65

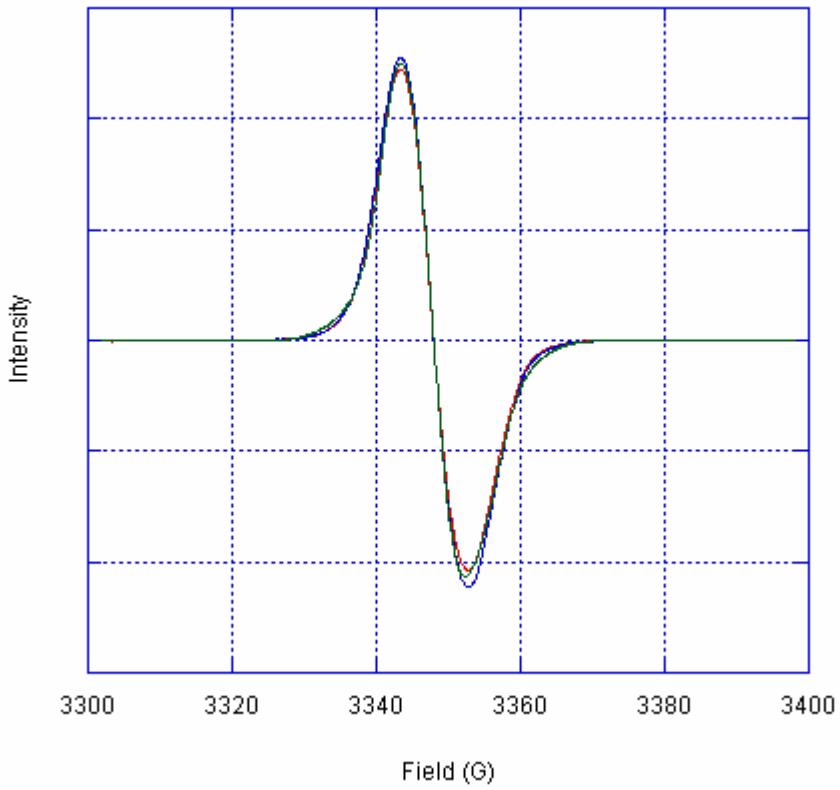

Figure 3.11 EPR Spectra of β, β'-d_2 Tyr-Cys· oxidized apoGAOX. The red solid line is the first experimental spectrum. The blue solid line is the second experimental spectrum and the green solid line is the XSophe simulated spectrum.

3.2.6 3, 5-d_2 Tyr-Cys· oxidized apoGAOX

3, 5-d_2 Tyr-Cys· oxidized apoGAOX (Figure 3.2e) contained ^{2}H on C5 with the ^{2}H on C3 replaced by a Cys residue. With a significant electron spin density on C3 and C5, the substitution of protons by ^{2}H led to a smaller spectral width (~55G) when compared to the unlabeled sample (~64G). XSophe simulation was performed after a ΔH_{corr} of +2.10G was applied to the EPR spectrum. The simulation was set up for a ^{12}C with anisotropic g-values, and two anisotropic hyperfine coupling constants for the two methylene protons. Since we have already determined the g-values, hyperfine coupling constants for the methylene protons in the previous analyses, those parameters could be transferred to this simulation. The simulated spectrum and the two experimental spectra are shown in Figure 3.12. The second experimental spectrum was very similar to the first spectrum after the frequency correction. The simulated spectrum was very close to the experimental spectra, giving rise to a set of spectral parameters (Table 3.6).

Table 3.6 Spectral parameter values for 3, 5-d_2 Tyr-Cys· oxidized apoGAOX at 50μW.

	g	$A_{\beta1}$ (G)	$A_{\beta2}$ (G)	Linewidth (G)
x	2.00740	14.69	8.68	3.06
y	2.00640	14.65	9.25	2.53
z	2.00211	14.33	8.08	2.26

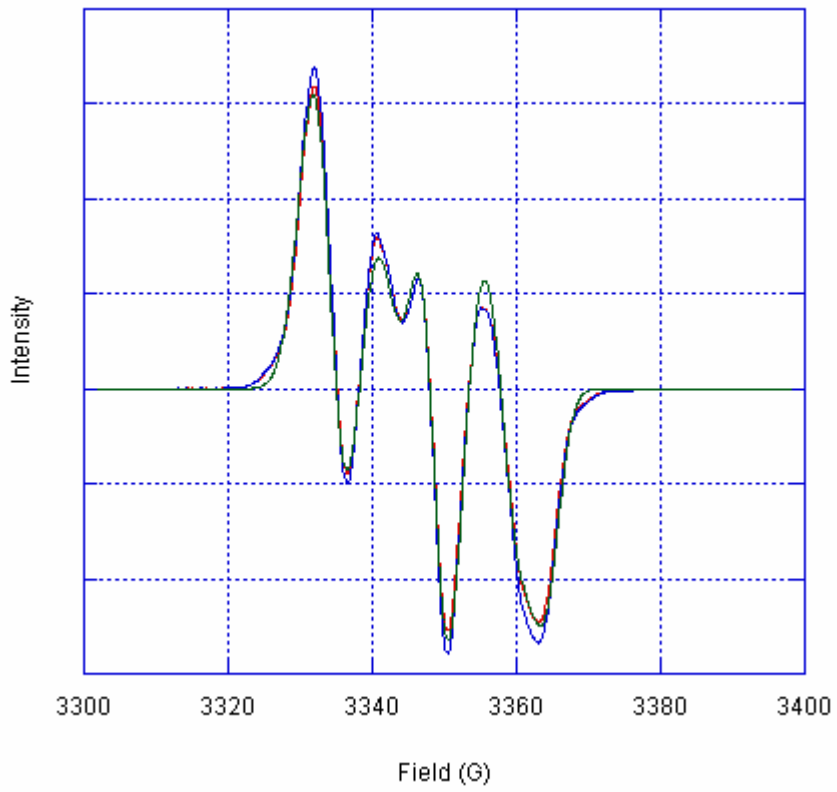

Figure 3.12 EPR Spectra of 3, 5-d_2 Tyr-Cys· oxidized apoGAOX. The red solid line is the first experimental spectrum. The blue solid line is the second experimental spectrum and the green solid line is the XSophe simulated spectrum.

3.2.7 2, 6-d_2 Tyr-Cys· oxidized ApoGAOX

2, 6-d_2 Tyr-Cys· oxidized apoGAOX (Figure 3.2d) contained two ^{2}H on C2 and C6. This substitution led to a decrease in the spectral width (~55G) when compared to the unlabeled sample (~64G). It also gave rise to a smaller linewidth at the low field side, causing a more resolved feature to form. XSophe simulation was performed after a ΔH_{corr} of +2.24G was applied to the EPR spectrum. The simulation was set up for a ^{12}C with anisotropic g-values, and two anisotropic hyperfine coupling constants for the two methylene protons. Transferring the known parameter values from the previous simulations helped determining the result in a more efficient way. The simulated spectrum and the two experimental spectra are shown in Figure 3.13. The second experimental spectrum was very similar to the first spectrum after applying the frequency correction. The simulated spectrum was very close to the experimental spectra, giving rise to a set of spectral parameters (Table 3.7).

Table 3.7 Spectral parameter values for 2, 6-d_2 Tyr-Cys· oxidized apoGAOX at 50μW.

	g	$A_{\beta1}$ (G)	$A_{\beta2}$ (G)	Linewidth (G)
x	2.00740	14.43	8.61	3.06
y	2.00640	14.53	9.00	3.41
z	2.00211	14.39	8.05	3.14

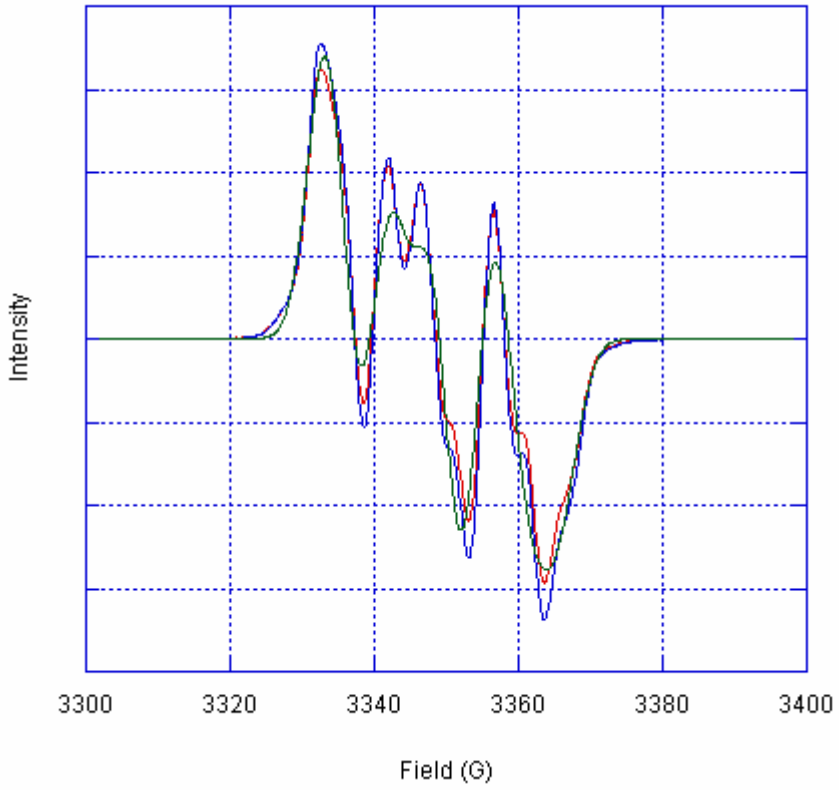

Figure 3.13 EPR Spectra of 2, 6-d_2 Tyr-Cys· oxidized apoGAOX. The red solid line is the first experimental spectrum. The blue solid line is the second experimental spectrum and the green solid line is the XSophe simulated spectrum.

3.2.8 Phenol-4-^{13}C Tyr-Cys· oxidized apoGAOX

In addition to the proton hyperfine interaction, ^{13}C could also give rise to hyperfine coupling due to its non-zero nuclear spin (I = ½). The extra hyperfine coupling broadened the spectrum of phenol-4-^{13}C Tyr-Cys· oxidized apoGAOX (Figure 3.2g) to ~61G with the appearance of new peak at the high field side. XSophe simulation was performed after a ΔH_{corr} of +2.15G was applied to the EPR spectrum to determine the hyperfine coupling constants of the ^{13}C on C4. The simulation was set up for a ^{13}C with anisotropic g-values, three anisotropic hyperfine coupling constants for the two methylene protons and the ^{13}C. The hyperfine coupling interaction from the ring protons were too small and could be neglected. Using the g-values and hyperfine coupling constants of methylene protons obtained in the previous analyses, the only unknown parameters were the hyperfine coupling constants of the ^{13}C. The simulated spectrum and the two experimental spectra are shown in Figure 3.14. The second experimental spectrum was as same as the first spectrum after applying the frequency correction. The simulated spectrum was very close to the experimental spectra, giving rise to a set of spectral parameters (Table 3.8).

Table 3.8 Spectral parameter values for phenol-4-^{13}C Tyr-Cys· oxidized apoGAOX at 50μW.

	g	$A_{\beta1}$ (G)	$A_{\beta2}$ (G)	A_{c1} (G)	Linewidth (G)
x	2.00710	14.21	8.01	9.52	3.05
y	2.00610	14.12	8.99	4.01	3.45
z	2.00210	13.81	7.60	3.50	3.97

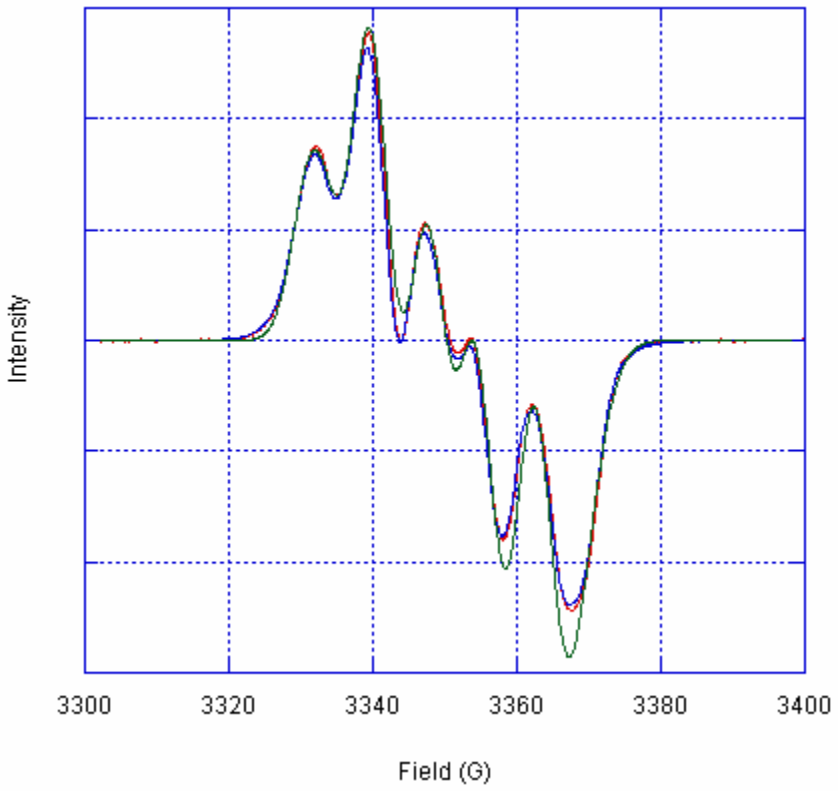

Figure 3.14 EPR Spectra of phenol-4-^{13}C Tyr-Cys· oxidized apoGAOX. The red solid line is the first experimental spectrum. The blue solid line is the second experimental spectrum and the green solid line is the XSophe simulated spectrum.

3.2.9 Phenol-3,5-$^{13}C_2$ Tyr-Cys· oxidized apoGAOX

Substitution of ^{12}C with ^{13}C at C3 and C5 led to a great increase in the spectral width (~76G) since C3 and C5 contained a significant electron density. A lot of the features in spectrum of phenol-4-^{13}C Tyr-Cys· oxidized apoGAOX were absent in the spectrum of phenol-3,5-$^{13}C_2$ Tyr-Cys· oxidized apoGAOX (Figure 3.2h) due to line broadening. XSophe simulation was performed after a ΔH_{corr} of +1.88G was applied to the EPR spectrum to determine the hyperfine coupling constants of the ^{13}C on C3 and C5. The simulation was set up for a ^{13}C with anisotropic g-values, four anisotropic hyperfine coupling constants for the two methylene protons and two ^{13}C. The hyperfine coupling interaction from the ring protons were too small and could be neglected. The simulated spectrum and the two experimental spectra are shown in Figure 3.15. The second experimental spectrum was as same as the first spectrum after applying the frequency correction. The simulated spectrum was very close to the experimental spectra, giving rise to a set of spectral parameters (Table 3.9).

Table 3.9 Spectral parameter values for phenol-3,5-$^{13}C_2$ Tyr-Cys· oxidized apoGAOX at 50μW.

	g	$A_{\beta1}$ (G)	$A_{\beta2}$ (G)	A_{c1} (G)	A_{c2} (G)	Linewidth (G)
x	2.00700	14.26	8.55	1.07	1.00	3.27
y	2.00610	14.16	8.99	1.07	1.01	3.47
z	2.00210	14.02	7.99	22.00	6.50	3.56

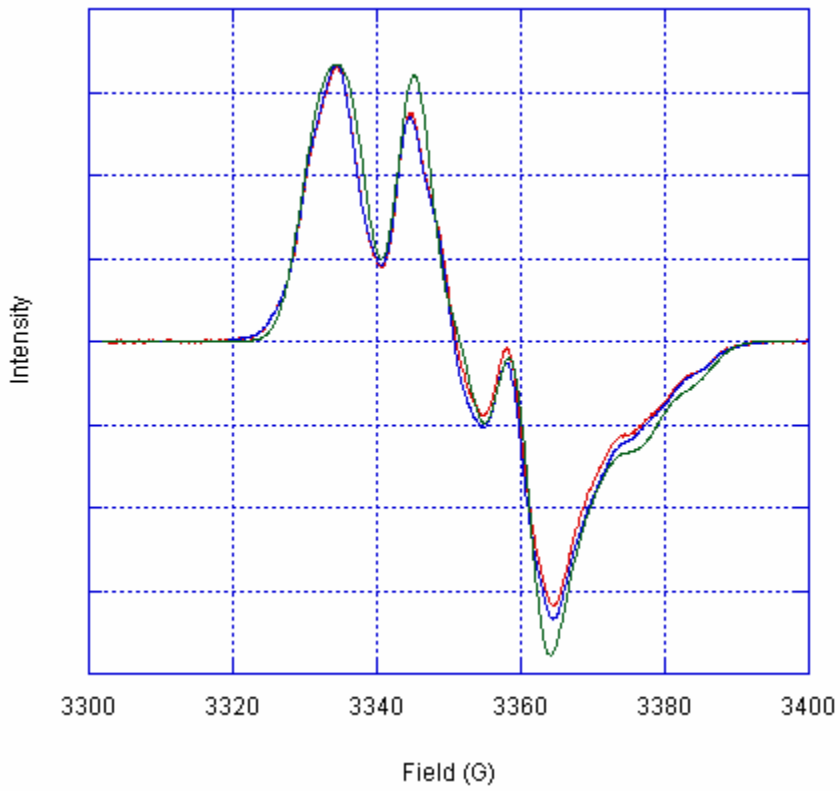

Figure 3.15 EPR Spectra of phenol-3,5-$^{13}C_2$ Tyr-Cys· oxidized apoGAOX. The red solid line is the first experimental spectrum. The blue solid line is the second experimental spectrum and the green solid line is the XSophe simulated spectrum.

3.2.10 ^{33}S Tyr-Cys· oxidized apoGAOX

Substitution of ^{32}S on Cys with ^{33}S resulted in hyperfine coupling. With the non-zero nuclear spin (I = 3/2) of ^{33}S, the spectrum was further split, so an extra peak appeared at the very high field end and line broadening happened at the low field region, causing spectral width to increase (~100G). The signal intensity of the spectrum was small when compared to the other samples because only 10-25% of free radical was delocalized on thioether sulfur and ^{33}S had a very small magnetogyric ratio. XSophe simulation was performed after a ΔH_{corr} of +2.14G was applied to the EPR spectrum to determine the hyperfine coupling constants of the ^{33}S. The simulation was set up for a ^{12}C with anisotropic g-values, three anisotropic hyperfine coupling constants for the methylene protons and ^{33}S. The simulated spectrum and the two experimental spectra are shown in Figure 3.16. The second experimental spectrum was as same as the first spectrum after applying the frequency correction. The simulated spectrum was very close to the experimental spectra, giving rise to a set of spectral parameters (Table 3.10).

Table 3.10 Spectral parameter values for ^{33}S Tyr-Cys· oxidized apoGAOX at 50μW.

	g	$A_{\beta 1}$ (G)	$A_{\beta 2}$ (G)	A_S (G)	Linewidth (G)
x	2.00710	14.46	8.67	1.98	3.17
y	2.00610	14.29	9.17	0.25	1.15
z	2.00200	14.04	7.73	16.01	3.29

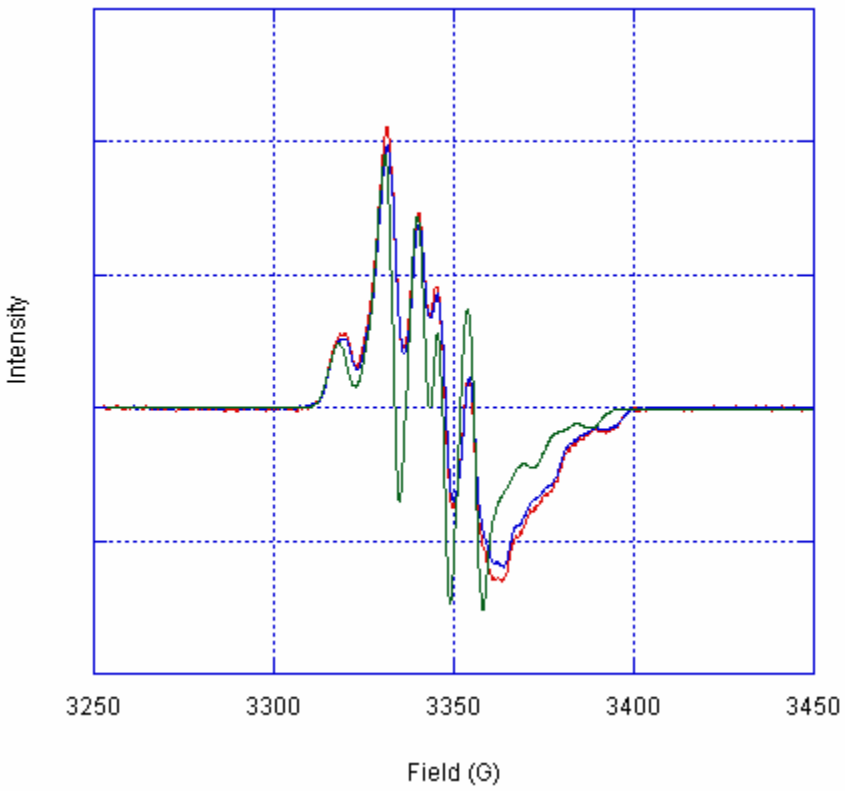

Figure 3.16 EPR Spectra of ^{33}S Tyr-Cys· oxidized apoGAOX. The red solid line is the first experimental spectrum. The blue solid line is the second experimental spectrum and the green solid line is the XSophe simulated spectrum.

3.2.11 ^{17}O Tyr-Cys· apoA GAOX

It has been suggested that significant unpaired electron density was found on Tyr phenoxyl oxygen. Therefore, replacing ^{16}O with ^{17}O would result in hyperfine interaction between the free radical and magnetic moment of oxygen, causing a great alternation to the spectrum from the unlabeled sample. ^{17}O contained a non-zero nuclear spin (I = 5/2), resulting in a multiplet splitting at the low and high field regions. Therefore, the spectral width was broadened to ~204G. However, the contribution of the hyperfine coupling from ^{17}O and its magnetogyric ratio were both smaller than the β protons, so the intensity of the multiplet structure at the low and high field regions were very small. The signals arising from the two methylene protons showed up as some sharp peaks around the center field (3350G) with narrow linewidths. XSophe simulation was performed after a ΔH_{corr} of +2.20G was applied to the EPR spectrum to determine the hyperfine coupling constants of the ^{17}O. The simulation was set up for a ^{12}C with anisotropic g-values, two anisotropic hyperfine coupling constants for the methylene protons and anisotropic hyperfine coupling constants for an oxygen nucleus which contained 50% ^{17}O and 50% ^{16}O. The simulated spectrum and the two experimental spectra are shown in Figure 3.17. The second experimental spectrum was as same as the first spectrum after applying the frequency correction. The simulated spectrum was very close to the experimental spectra, giving rise to a set of spectral parameters (Table 3.11).

Table 3.11 Spectral parameter values for ^{17}O Tyr-Cys· oxidized apoGAOX at 50μW.

	g	$A_{\beta1}$ (G)	$A_{\beta2}$ (G)	A_O(G)	Linewidth (G)
x	2.00710	14.75	9.00	1.00	3.00
y	2.00610	14.68	9.57	1.00	3.00
z	2.00210	14.30	8.11	31.70	3.00

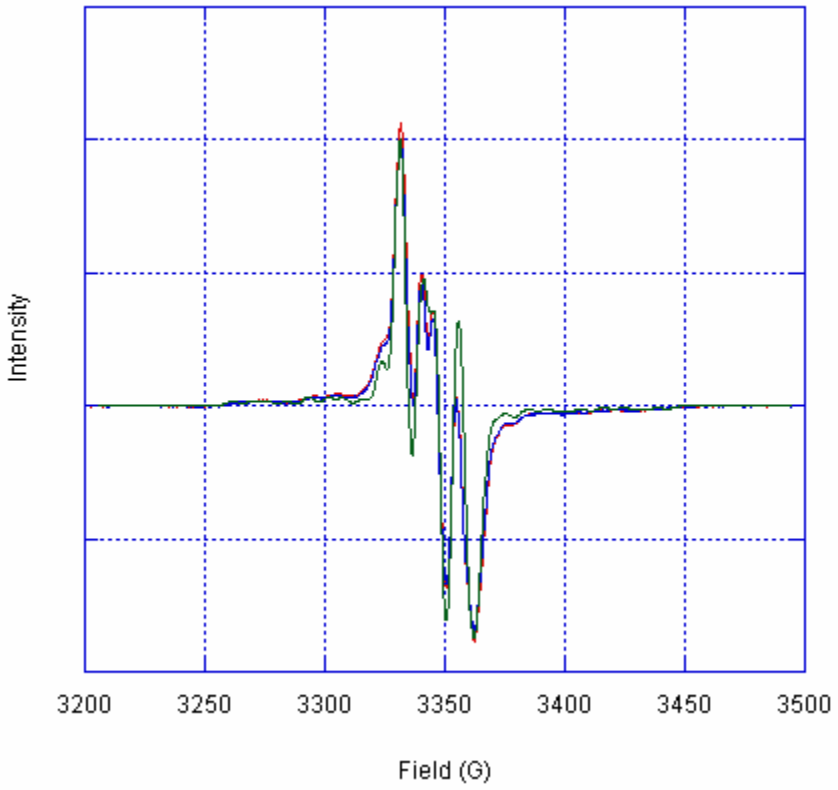

Figure 3.17 EPR Spectra of ^{17}O Tyr-Cys· oxidized apoGAOX. The red solid line is the first experimental spectrum. The blue solid line is the second experimental spectrum and the green solid line is the XSophe simulated spectrum.

CHAPTER 4
DISCUSSION

4.1 ^2H Isotopic Labeling

Deuteration can reduce the large proton hyperfine coupling by a factor of ~6.5 according to the magnetogyric ratio. In perdeuterated Tyr-Cys· apoA GAOX, all of the protons are replaced with ^2H, resulting in the diminishment of the hyperfine splitting. Therefore, the spectral shape is determined mainly by the g-anisotropy. Even though the ^2H hyperfine coupling constants are small, if they are not included in the simulation, a minor shift in the g-values occurs. Moreover, the broad linewidths obtained from the calculation are the consequence of the absence of hyperfine coupling constants, since the calculation is trying to compensate for the lost of hyperfine coupling by broadening the linewidths, which will lead to an inaccurate result. As shown in Table 3.1, our g-values are the same as previously reported within the experimental error. According to Gerfen's article (23), their g-values for oxidized apoGAOX are 2.00741, 2.00641, and 2.00211, which are not as same as the values that we obtained. However, the addition of methylene proton hyperfine coupling constants in the simulation results in a set of g-values (Table 3.4) closer to the published values and narrower linewidths since the calculation is more similar to the reality and so the result is more accurate. The g-values are very consistent in other ^2H-labeled samples as well, except those for the β, β'-H_2 Tyr-Cys· oxidized apoGAOX (Table 3.3). But after considering the experimental error, our values are still acceptable.

In GAOX, the hyperfine splitting mainly comes from the two methylene protons (H_β). Hence, deuteration of all the ring protons in β, β'-H_2 Tyr-Cys· oxidized apoGAOX can simplify the EPR spectrum and the determination of hyperfine coupling constants arising from the two H_β will be more straightforward. XSophe simulation gives rise to two sets of proton hyperfine coupling constants, and they are very similar to the published values (23, 24). The simulation of β, β'-d_2 Tyr-Cys· oxidized apoGAOX also shows that the hyperfine coupling constants for the methylene ^2H stay in the range of the expected values (A_{proton} / 6.5). The simulated spectrum of 3,5- d_2 Tyr-Cys· and 2,6-d_2 Tyr-Cys· oxidized apoGAOX fits nicely with the experimental spectrum with a set of parameter values very close to the literature values.

Based on the calculation performed by the Svistunenko and Cooper's program (25), two sets of solutions are obtained (Figure 3.9), which correspond to two different electron spin density on C1 (0.278 and 0.802). Since this program is designed for calculating the rotation angle and the electron spin density on C1 of tyrosyl radicals, but not tyrosyl-cysteine radicals, the result is compared with the electron spin density calculated for unsubstituted tyrosyl radicals. The electron spin density on C1 calculated by Gerfen (23) is 0.26, which is very close to one of our solutions (0.278). Moreover, from on the crystal structure of galactose oxidase (PDB ID 1gog), the dihedral angle of the methylene proton for Tyr272 were -43.9^o. Using Svistunenko's program, the hyperfine coupling constants from this dihedral angle are confirmed to be the same as the ones we used (8.89G and 14.56G). Therefore, the first set of solutions with 0.278 electron spin density is more valid.

The presence of high power component is proven by the simulation for the high power EPR spectrum of perdeuterated Tyr-Cys· sample. Rhombic g-values are determined by the simulation, and they are very different from what we obtained for the perdeuterated Tyr-Cys· oxidized sample collected at low power, indicating that the g-values might come from another Tyr derived free radical in the sample. However, since this high power component is a minor species, so we chose not to investigate it further.

4.2 ^{13}C Isotopic Labeling

In the unlabeled sample, ^{12}C is EPR silent because it possesses a zero nuclear spin. Substitution of ^{12}C with ^{13}C (I = ½) results in hyperfine coupling interaction and more information on the electron spin density can be obtained. Phenol-4-^{13}C Tyr-Cys· apoA GAOX is an important sample for us to determine the spin density on C4 since C4 doesn't have a proton attached to it, so hyperfine coupling interaction from ^{13}C is necessary. The g-values deviate slightly from the other values, but they are still within the error range. Surprisingly, The g-values of phenol-3,5-$^{13}C_2$ Tyr-Cys· oxidized apoGAOX are very similar to the ones of phenol-4-^{13}C Tyr-Cys· sample. It means that the apparent shift in g-values in both the phenol-4-^{13}C Tyr-Cys· and phenol-3,5-$^{13}C_2$ Tyr-Cys· samples is due to the same factor, which might be the neglect of the hyperfine coupling constants for the ring protons in the calculation.

The hyperfine coupling constants of the methylene protons for the ^{13}C-labeled samples are very similar to those we obtained from the ^{2}H-labeling analyses, reflecting the accuracy of the result obtained from XSophe simulation. The hyperfine coupling constants of the ring ^{13}C are also determined by XSophe from the two ^{13}C-labeled samples. It shows that the A_z hyperfine coupling arising from C4 is not very large, indicating that the electron spin density on C4 is relatively small. In contrast, the hyperfine coupling constants arising from C3 and C5 are larger. It is due to the significant electron spin density on C3 and C5. This result is consistent with calculated electron spin density map of the Tyr-Cys free radical in the ground state (Figure 1.5), having significant electron spin density on the alternating ring carbons. Moreover, the hyperfine coupling constants of the z component for the two ring ^{13}C are obviously larger than the x and y components since the $2p_z$ orbital of the ring carbon are involved in the aromatic π system, which contained a more significant electron spin density than the other two orbitals.

4.3 ^{17}O and ^{33}S Isotopic Labeling

After working on the ring atoms- carbon and hydrogen, we can finally perform some analyses on two exocyclic atoms- oxygen and sulfur. Computational studies show that high electron spin density is found on phenoxyl oxygen and thioether sulfur, so it is worthwhile to interpret those positions by synthesizing ^{17}O-labeled and ^{33}S-labeled samples. ^{17}O and ^{33}S both contain a non-zero nuclear spin, resulting in hyperfine interaction. This additional hyperfine coupling gives rise to a big change to the EPR spectra. For the ^{33}S-labeled and ^{17}O-labeled sample, the g-values obtained from the simulation were very similar to the ones we use for the ^{13}C samples because the simulations of these samples also do not include the hyperfine coupling constants of the ring protons.

The hyperfine coupling constants for the methylene protons of both the ^{33}S- and ^{17}O-labeled samples were consistent with the ones that we obtained from the ^{2}H- and ^{13}C-labeled samples, it further enhances our confidence on the results. The simulation also gives rise to the hyperfine coupling constants for the ^{33}S and ^{17}O. A large A_z of ^{33}S and ^{17}O are obtained and it indicates that a significant amount of electron spin density was found in the $2p_z$ orbital of both sulfur and oxygen. This result is also consistent with calculated electron spin density map of the Tyr-Cys free radical (Figure 1.5), which indicates that major electron spin density is localized on thioether sulfur and phenoxyl oxygen.

CHAPTER 5
CONCLUSION

The analysis shows that a systematic simulation of a family of isotopic variants can determine the spectral parameters in an accurate and efficient way by repeating the optimization process for each sample in order to refine the parameter values and producing the high quality of fit for the experimental spectra. In our analysis, none of the ring protons or deuterons is included in the calculation and it may lead to the deviation from the true values, so I believe that including the hyperfine coupling constants from the ring protons or deuterons will further improve the spectral parameter values obtained from the simulation and the best result will eventually arise when the parameter values for all the samples are consistent. Moreover, using an EPR spectrum that contains only the signal from Tyr-Cys· free radical can help improving the result of the simulation. Since all of our low power spectra contain a certain amount of signal from the high power component, elimination of the signal from the high power component can be achieved by subtracting the high power EPR spectrum from the low power EPR spectrum with a normalization constant included. From the high power spectrum, we can also determine the identity of the high power species by XSophe simulation. It enables us to understand not only the free radical site, but also the environment around the active site.

The magnitude of the hyperfine coupling constants from each of the atoms can confirm that significant electron spin density is found on the methylene protons, the alternating atoms within the aromatic π system, the thioether sulfur and the phenoxyl oxygen. Further analysis should be performed for $^{13}C_6$ ring Tyr-Cys· apoA GAOX to

obtain a complete set of spectral parameters for all of the nuclei in the Tyr-Cys· side chain, so that a satisfactory and complete unpaired electron spin density distribution can be mapped out.

REFERENCES

[1] Lander, Harry M. **An essential role for free radicals and derived species in signal transduction.** *The FASEB Journal.* **11**, 118-124. (1997)

[2] Faller, Peter, Debus, Richard J., Brettel, Klaus, Sugiura, Miwa, Rutherford, A. William, Boussac, Alain. **Rapid formation of the stable tyrosyl radical in photosystem II.** *PNAS.* **98**, 14368-14373. (2001)

[3] Miller, M. A., Han, G. W., Kraut, J. **A cation binding motif stabilizes the compound I radical of cytochrome *c* peroxidase.** *PNAS.* **91,** 11118–11122. (1994)

[4] Bertini, Ivano, Gray, Harry B., Stiefel, Edward I., Valentine, Joan Selverstone. **Biological Inorganic Chemistry Structure and Reactivity.** *University Science Books, United States of America.* 557-561. (2007)

[5] Whittaker, James W. **Galactose Oxidase.** *Advances in Protein Chemistry.* **60**, 1-49. (2002)

[6] Firbank, S.J., Rogers, M.S., Wilmot, C.M., Dooley, D.M., Halcrow, M.A., Knowles, P.F., McPherson, M.J., Phillips, S.E.V. **Crystal structure of the precursor of galactose oxidase: An unusual self-processing enzyme.** *PNAS.* **98,** 12932-12937. (2001)

[7] Whittaker, James W. **Free Radical Catalysis by Galactose Oxidase.** *Chemical Reviews.* **103**, 2347-2363. (2002)

[8] Ito, N., Phillips, S.E.V., Stevens, C., Ogel, Z.B., McPherson, M.J., Keen, J.N., Yadav, K.D.S., Knowles, P.F. **Novel thioether bond revealed by a 1.7Å crystal structure of galactose oxidase.** *Letters to Nature.* **350**, 87-90. (1991)

[9] Whittaker, Mei M., Whittaker, James W. **Cu(I)-dependent Biogenesis of the Galactose Oxidase Redox Cofactor.** *The Journal of Biological Chemistry.* **278**, 22090-22101. (2003)

[10] Vaidyanathan, M., Palaniandavar, M. **Models for the active site in galactose oxidase: Structure, spectra and redox of Copper(II) complexes of certain phenolate ligands.** *Proc. Indian Acad. Sci. (Chem. Sci.).* **112**, 223-238. (2000)

[11] Wertz, John E., Bolton, James R. **Electron Spin Resonance Elementary Theory and Practical Applications.** *McGraw-Hill, Inc, United States of America.* 30-32. (1972)

[12] Lund, Anders, Shiotana, Masaru. **EPR of Free Radicals in Solids.** *Progress in Theoretical Chemistry and Physics.* **10**, 1-25. (1993)

[13] Drago, Russell S. **Physical Methods For Chemists.** 2nd ed**.** *Saunders College Publishing, Mexico.* 370-374. (1992)

[14] Hales, Brian J. **Intrinsic and Extrinsic Paramagnets as Probes of Metal Clusters.** *Methods in Enzymology*. **227**, 384-395. (1993)

[15] Whittaker, Mei M., Whittaker, James W. **Construction and characterization of *Pichia pastoris* strains for labeling aromatic amino acids in recombinant proteins.** *Protein Expression and Purification.* **41**, 266-274. (2005)

[16] Griffiths, D.V., Fecney, J., Roberts, G.C.K., and Burgen, A.S.V. **Preparation of selectivity deuterated aromatic amino acids for use in 1H NMR studies of proteins.** *Biochimica et Biophysica Acta.* **446**, 479-485. (1976)

[17] **Yeast Media.** Revised: 2007. *Clontech.* Available: http://www.clontech.com/products/detail.asp?tabno=2&product_id=10615 [Viewed: June 19, 2007].

[18] Whittaker, Mei M., Whittaker, James W. **Expression of Recombinant Galactose Oxidase by *Pichia pastoris.*** *Protein Expression and Purification.* **20**, 105-111. (2000)

[19] Amaral, D., Bernstein, L., Morse, D., Horecker, B. L. *The Journal of Biological Chemistry*. **238**, 2281-2284. (1963)

[20] Whittaker, Mei M., Whittaker, James W. **A Tyrosine-derived Free Radical in Apogalactose Oxidase.** *The Journal of Biological Chemistry*. **265**, 9610-9613. (1990)

[21] Tsai, A-L., Berka, V., Chen, P.-F., Palmer, G. **Characterization of Endothelial Nitric-oxide Synthase and Its Reaction with Ligand by Electron Paramagnetic Resonance Spectroscopy.** *The Journal of Biological Chemistry*. **271**, 32563-32571. (1996)

[22] Hanson, Graeme R., Gates, Kevin E., Noble, Christopher J., Griffin, M., Mitchell, A., Benson, S. **XSophe-Sophe-XeprView®. A computer simulation software suite (v.1.1.3) for the analysis of continuous wave EPR spectra.** *Journal of Inorganic Biochemistry*. **98,** 903-916. (2004)

[23] Gerfen, Gary J., Bellew, Brendan F., Griffin, Robert G., Singel, David J., Ekberg, Christopher A., Whittaker, James W. **High-Frequency Electron Paramagnetic Resonance Spectroscopy of the Apogalactose Oxidase Radical.** *Journal of Physical Chemistry*. **100**, 16739-16748. (1996)

[24] Hulsebosch, R.J., van Den Brink, J.S., Nieuwenhuis, S.A.M., Gast, P., Raap, J., Lugtenburg, J., Hoff, A.J. **Electronic Structure of the Neutral Tyrosine Radical in**

Frozen Solution. Selective ^{2}H-, ^{13}C-, and ^{17}O-Isotope Labeling and EPR Spectroscopy at 9 and 35GHz. *J. Am. Chem. Soc.* **119**, 8685-8694. (1997)

[25] Svistunenko, Dimitri A., Cooper, Chris E. **A New Method of Identifying the Site of Tyrosyl Radicals in Proteins.** *Biophysial Journal.* **87**, 582-595. (2004)

BIOGRAPHICAL SKETCH

I was born in Hong Kong on August 11th, 1983 and I moved to the United States with my family in 2000. I received my Bachelor degree in Biochemistry at University of Oregon in 2005. After that, I have been working toward my Master degree in Biochemistry and Molecular Biology in the lab of Dr. James Whittaker at OGI School of Science & Engineering of Oregon Health and Science University. My research interests are free radicals and antioxidants.